A HIGH-RESOLUTION SPECTROSCOPIC SEARCH FOR THE REMAINING DONOR FOR TYCHO'S SUPERNOVA

WOLFGANG E. KERZENDORF[1,2], DAVID YONG[1], BRIAN P. SCHMIDT[1], JOSHUA D. SIMON[3], C. SIMON JEFFERY[4], JAY ANDERSON[5], PHILIPP PODSIADLOWSKI[6], AVISHAY GAL-YAM[7], JEFFREY M. SILVERMAN[8,9], ALEXEI V. FILIPPENKO[8], KEN'ICHI NOMOTO[10], SIMON J. MURPHY[1], MICHAEL S. BESSELL[1], KIM A. VENN[11], AND RYAN J. FOLEY[12]

[1] Research School of Astronomy and Astrophysics, Mount Stromlo Observatory, Cotter Road, Weston Creek, ACT 2611, Australia; wkerzend@mso.anu.edu.au
[2] Department of Astronomy and Astrophysics, University of Toronto, 50 Saint George Street, Toronto, ON M5S 3H4, Canada
[3] The Observatories of the Carnegie Institution for Science, 813 Santa Barbara Street, Pasadena, CA 91101, USA
[4] Armagh Observatory, College Hill, Armagh BT61 9DG, UK
[5] Space Telescope Science Institute, Baltimore, MD 21218, USA
[6] Department of Astrophysics, University of Oxford, Oxford, OX1 3RH, UK
[7] Benoziyo Center for Astrophysics, Faculty of Physics, The Weizmann Institute of Science, Rehovot 76100, Israel
[8] Department of Astronomy, University of California, Berkeley, CA 94720-3411, USA
[9] Department of Astronomy, University of Texas, Austin, TX 78712-0259, USA
[10] Kavli Institute for the Physics and Mathematics of the Universe, The University of Tokyo, 5-1-5 Kashiwanoha, Kashiwa, Chiba 277-8583, Japan
[11] Department of Physics and Astronomy, University of Victoria, Elliott Building, 3800 Finnerty Road, Victoria, BC V8P 5C2, Canada
[12] Harvard-Smithsonian Center for Astrophysics, 60 Garden Street, Cambridge, MA 02138, USA

ABSTRACT

In this paper, we report on our analysis using *Hubble Space Telescope* astrometry and Keck-I HIRES spectroscopy of the central six stars of Tycho's supernova remnant (SN 1572). With these data, we measured the proper motions, radial velocities, rotational velocities, and chemical abundances of these objects. Regarding the chemical abundances, we do not confirm the unusually high [Ni/Fe] ratio previously reported for Tycho-G. Rather, we find that for all metrics in all stars, none exhibit the characteristics expected from traditional Type Ia supernova single-degenerate-scenario calculations. The only possible exception is Tycho-B, a rare, metal-poor A-type star; however, we are unable to find a suitable scenario for it. Thus, we suggest that SN 1572 cannot be explained by the standard single-degenerate model.

Key words: ISM: supernova remnants – supernovae: individual (SN1572)

Online-only material: color figures

1. INTRODUCTION

Type Ia supernovae (SNe Ia) are of great interest. They represent some of the most extreme physical situations in stellar astronomy, control the chemical evolution of galaxies and the universe at intermediate to late times by producing large amounts of iron-group elements, and are uniquely powerful cosmic distance probes. But despite their wide-ranging significance, fundamental uncertainties remain around the progenitors of these cataclysmic events.

There is a general consensus that SNe Ia are caused by the deflagration/detonation of a carbon–oxygen white dwarf which is accreting material from a binary companion. Scenarios exist where the explosion can be initiated from a detonation on the surface of the star (Livne & Arnett 1995; Fink et al. 2010), through runaway carbon burning in the white dwarf's interior, or through a cataclysmic merger of objects.

Observationally, two main models for this accretion process can be identified. The single-degenerate scenario (SD-scenario) sees the accretion process occurring through Roche-lobe overflow (RLOF) of a close nondegenerate companion (also known as a donor star). This companion, which has undergone common-envelope evolution with the white dwarf, can be a helium, main-sequence, subgiant, or red giant star. In all cases, the donor star should survive the explosion (except for possibly in the case of the helium-star donor; R. Pakmor 2012, private communication) and remain visible post-explosion.

The second scenario is the dynamical merger of two white dwarfs, known as the double-degenerate scenario. In this scenario, the coevolution of two stars eventually leads to a close binary of two white dwarfs, which are able, through the emission of gravitational radiation, to merge over a wide range of times after the initial formation of the system. In most cases, this would leave no remaining star (e.g., Pakmor et al. 2010).

Both scenarios have support in observations and theory. The detection of circumstellar material around certain SNe Ia (Patat et al. 2007; Simon et al. 2009; Sternberg et al. 2011; Foley et al. 2012) provides evidence for the SD-scenario. On the other hand, the lack of substantial hydrogen in the majority of other SNe Ia (Leonard 2007) poses a challenge to the SD-scenario.

Kasen (2010) suggests that the interaction of the shock wave with the nondegenerate companion should result in a light excess at early times of an SN Ia light curve, which depends on the viewing angle and the companion radius. Such an excess has not yet been observed (Hayden et al. 2010; Tucker 2011; Bianco et al. 2011; Ganeshalingam et al. 2011), which is at odds with red giant companions forming the majority of SNe Ia. Justham (2011), Di Stefano et al. (2011), and Hachisu et al. (2012a, 2012b), however, have suggested a scenario where the white dwarf is spinning and thus can accrete above the Chandrasekhar limit. The explosion would only occur once the white dwarf had spun down sufficiently, which would give the red giant a chance to evolve and would not require the detection of the early excess in the light curve in a red giant progenitor scenario.

Population-synthesis calculations are challenging, with various authors getting different results for the same inputs. However, there is a general trend from these calculations that neither single-degenerate nor double-degenerate stars can

provide enough systems to explain the observed SN Ia rate (Han 2008; Ruiter et al. 2009; Mennekens et al. 2010; Yu & Jeffery 2010). Several authors suggest that the population might comprise both single-degenerate and double-degenerate systems.

The physics of white-dwarf mergers is challenging to simulate numerically, but in the simplest calculations, these mergers lead to the formation of a neutron star via electron capture, rather than to a thermonuclear explosion (Saio & Nomoto 1985). Recently, Pakmor et al. (2010) have shown that for certain parameters (white-dwarf binaries with a mass ratio very close to one) the merger may explain subluminous supernovae (SNe; e.g., SN 1991bg; see Filippenko 1997, for a review), although Dan et al. (2011) note that the initial conditions of the system may change these conclusions.

SN 2011fe was detected only ∼11 hr after the explosion (Nugent et al. 2011), and (with a distance of 6.4 Mpc) is one of the closest SNe Ia ever found. Nugent et al. (2011) and Brown et al. (2012) have not found any early-time light-curve excess predicted by Kasen (2010), and thus rule out a red giant donor. Radio and X-ray observations by Horesh et al. (2012) show no strong signs of pre-explosion outflows, which again contradicts a red giant scenario for SN 2011fe. Additional radio measurements by Chomiuk et al. (2012) suggest a low density around SN 2011fe, which is at odds with many conventional SD-scenarios. Li et al. (2011) have searched pre-explosion archival images and can also rule out luminous red giants and almost all helium stars as donors. In addition, Bloom et al. (2012) have used images believed to have been taken 4 hr post-explosion and suggest the companion radius to be less than 0.1 $R_\odot$. Most of these results are consistent with a main-sequence companion or a white-dwarf companion.

Because it is very difficult to obtain robust constraints on the progenitor system in the immediate aftermath of a 10^{51} erg explosion, an alternative is to study somewhat older and more nearby SNe that can be observed in great detail. Ruiz-Lapuente et al. (2004, henceforth RP04) have tried to directly detect donor stars in old and nearby SN Ia remnants within the Milky Way. They have identified two historical Galactic SNe well suited to this task—SN 1006 and SN 1572 (Tycho's SN). Both remnants are young (1000 and 440 yr old, respectively), closeby (2.2 ± 0.08 kpc, Winkler et al. 2003; 2.8 ± 0.8 kpc, Ruiz-Lapuente 2004), almost certainly SNe Ia from their observational signatures (Badenes et al. 2006; Ruiz-Lapuente 2004; Krause et al. 2008; Rest et al. 2008), and not overwhelmed by Galactic extinction. In this paper, we will focus on SN 1572.

RP04 investigated most bright stars in the central region of SN 1572 and found a star with an unusual spatial motion (Tycho-G by their nomenclature); they suggested this as a possible donor star for SN 1572. While the star has an unusual spatial motion compared to other stars in the field, its current location and proper motion place it on a significant distance from the center of the supernova remnant (SNR)—a feature difficult to explain in connecting Tycho-G to SNR 1572.

In the case of RLOF, the time scale for synchronization of the orbit by tidal interaction due to dissipation processes is short enough to ensure almost synchronous rotation in spite of mass-loss. This results in an unusually large rotational velocity, related to the orbital velocity of the binary system, and it might be used to single out possible donor stars from nearby unrelated stars. Kerzendorf et al. (2009, henceforth WEK09) investigated the rotation of Tycho-G but found no excess rotational velocity compared to a normal star. A comparison of

WEK09's measurements of Tycho-G, including a revised radial velocity $v_{\rm rad}$, with Galactic kinematic models showed that it is statistically consistent with an unrelated thick/thin-disk star. However, WEK09 were able to provide an a priori unlikely donor-star scenario, where the star was able to lose its rotational signature.

González Hernández et al. (2009, henceforth GH09) analyzed a spectrum of Tycho-G observed with the High Resolution Echelle Spectrometer (HIRES; Vogt et al. 1994) instrument on the Keck-I 10 m telescope, finding a $v_{\rm rad}$ value consistent with WEK09's revised $v_{\rm rad}$. They also measured the stellar parameters and metallicity of Tycho-G, concluding that it has an unusually high nickel abundance, which they claim can be attributed to the accretion of ejecta material on the donor star during the explosion.

In this paper, we analyze HIRES spectra of the six bright stars near the center of SNR 1572. These spectra were taken as part of the same program that obtained the data used by GH09, and we independently reanalyze the Tycho-G spectrum in our program. We describe the observational data and our data-reduction procedures in Section 2. Section 3 is divided into six subsections detailing the measurements of proper motion, radial velocity, rotation, stellar parameters, and abundances, and we provide a detailed comparison between our and GH09's measurements of Tycho-G. In Section 4, we analyze the measurements of each star to investigate its potential association with SNR 1572, and we present our conclusions in Section 5.

2. OBSERVATIONS AND DATA REDUCTION

We obtained spectra with the HIRES spectrograph on the Keck-I telescope on Mauna Kea. The observations were made on 2006 September 10 and 2006 October 11 UT. Slits B5 and C1 (width 0″86; B5 length 3″5, C1 length 7″0) were used, resulting in wavelength coverage of 3930–5330 Å, 5380–6920 Å, and 6980–8560 Å with $R = \lambda/\Delta\lambda \approx 50,000$, providing us with the necessary spectral resolution and wavelength coverage to determine stellar parameters.

The spectra were reduced using the MAKEE package. All spectra were corrected to heliocentric velocities, using the MAKEE sky-line method. The spectra were not corrected for telluric absorption lines, but only regions known to be free from telluric contamination were used in the analysis to derive the stellar parameters. The final exposure times of the combined spectra for each candidate and the signal-to-noise ratio (S/N) at 5800–5900 Å are shown in Table 1. Finally, we normalized the spectrum using the IRAF[13] task CONTINUUM. We note that Tycho-C and Tycho-D were observed on the same slit (C1); they are separated by 2″1, and the seeing was ∼0″8, with Tycho-C being roughly five times brighter than Tycho-D. All HIRES spectra (except Tycho-B) are available for download in the WISEREP repository (http://www.weizmann.ac.il/astrophysics/wiserep; Yaron & Gal-Yam 2012).

In addition, we obtained low-resolution spectra ($R \approx 1200$) of Tycho-B with the dual-arm Low-Resolution Imaging Spectrometer (LRIS; Oke et al. 1995) mounted on the Keck-I telescope. The data were taken on 2010 November 7 UT, using only the blue arm with the 600/4000 grism and the 1″ wide slit. This resulted in a wavelength coverage of 3200–5600 Å. These data

---

[13] IRAF is distributed by the National Optical Astronomy Observatory, which is operated by the Association of Universities for Research in Astronomy, Inc., under cooperative agreement with the National Science Foundation.

Table 1
Observations

Tycho (Name)	α(J2000) (hh:mm:ss.ss)	δ(J2000) (dd:mm:ss.ss)	Date (dd/mm/yy)	Slit	t_{exp} (minutes)	V[a] (mag)	S/N[b]
A	00:25:19.73	+64:08:19.60	10/09/06	B5	15	13, 29	~48
B	00:25:19.95	+64:08:17.11	10/09/06	B5	20	15.41	~45
C	00:25:20.40	+64:08:12.32	11/10/06	C1	180	19.06[c]	~8
D	00:25:20.60	+64:08:10.82	11/10/06	C1	180	20.70	~3
E	00:25:18.29	+64:08:16.12	11/10/06	C1	150	19.79	~9
G	00:25:23.58	+64:08:02.06	10/09/06 & 11/10/06	B5&C1	400	18.71	~25

Notes.

[a] Magnitudes from RP04.

[b] The S/N value was obtained by measuring the root mean square of the pixels (each resolution element is sampled by two pixels) in continuum regions near 5800–5900 Å. For the purposes of measuring the stellar parameters, the spectrum was convolved so that the S/N increased by a factor of 2.24.

[c] RP04 notes that this is an unresolved pair with a brighter bluer component ($V = 19.38$ mag) and a fainter redder component ($V = 20.53$ mag).

were taken to obtain a precise measurement of the surface gravity for Tycho-B using the observed Balmer decrement (Bessell 2007).

The spectrum of Tycho-B was reduced using standard techniques (e.g., Foley et al. 2003). Routine CCD processing and spectrum extraction were completed with IRAF, and the data were extracted with the optimal algorithm of Horne (1986). We obtained the wavelength scale from low-order polynomial fits to the calibration-lamp spectra. Small wavelength shifts were then applied to the data after measuring the offset by cross-correlating a template sky to the night-sky lines that were extracted with the star. Using our own IDL routines, we fit a spectrophotometric standard-star spectrum to the data in order to flux calibrate Tycho-B and remove telluric lines (Horne 1986; Matheson et al. 2000).

3. ANALYSIS

3.1. Astrometry

Proper motions can be used to identify potential donor stars because donor stars freely travel with their orbital velocity after the SN explosion disrupts the system. RP04 suggested Tycho-G as a possible donor due to its unusually high values for both the proper motion and the radial velocity. For this work, we measured proper motions for 201 stars within 1 arcmin of the remnant's center. We used archival *Hubble Space Telescope* (*HST*) images for three different epochs (*HST* Programs GO-9729 and GO-10098; 2003 November, 2004 August, 2005 May), each consisting of three depths with three exposures each (3×0.5 s, 3×10 s, 4×480 s) with the F555W filter using the Advanced Camera for Surveys. The scale in each exposure is 50 mas pixel^{-1}. This data set results in a maximum baseline of 18 months.

We used an image from the middle epoch (2004) to establish a reference frame and oriented the pixel coordinate system with the equatorial system. We then applied a distortion correction for the F555W filter (Anderson & King 2006) and calculated transformations between all other images and the reference image. Next, we extracted the stellar positions in all frames (utilizing a library point-spread function that varies across the field) and used the transformations between the images to calculate the position of all stars in the reference coordinate system, with the overall uncertainty of each position estimated. Some faint stars were not detected in the shorter exposures and

were thus excluded from proper-motion measurements. In total, 114 stars were used in the astrometric analysis.

For each star, we fit a linear regression for the stellar positions over time in the pixel coordinates (which were aligned with the equatorial system). The *x* and *y* data were treated as independent measurements, with separate regressions solved for each axis direction. Uncertainties were estimated using standard least-squares analysis and the individual uncertainty estimates of each object's positions.

There are three J2000 measurements of the geometric center of SN 1572 from different data sets. Reynoso et al. (1997) used Very Large Array data to find $\alpha = 00^{\mathrm{h}}25^{\mathrm{m}}14\overset{s}{.}95$, $\delta = +64°08'05''.7$; Hughes (2000) used *ROSAT* data to measure $\alpha = 00^{\mathrm{h}}25^{\mathrm{m}}19\overset{s}{.}0$, $\delta = +64°08'10''$; and Warren et al. (2005) used *Chandra X-Ray Observatory* data to get $\alpha = 00^{\mathrm{h}}25^{\mathrm{m}}19\overset{s}{.}40$, $\delta = 64°08'13''.98$. We note that the X-ray centers agree rather well with a difference of less than $5''$, but the radio center is located roughly $30''$ away from the X-ray centers. Thus, we believe the uncertainty in the geometric center is rather large (of the order of $30''$).

Table 2 lists the proper motions and uncertainties of all stars mentioned by RP04 (19 stars) that were analyzed in this work, as well as the distance to the geometric X-ray center measured by *Chandra*.

We note that Tycho-2 has a relatively high proper motion, but its position in the year 1572 was $67''.95$ away from the remnant's center, and we thus exclude it as a viable candidate for the donor.

In Figure 1, we compare the distribution of proper motions of all measured stars with those of our candidates. All of the latter are reconcilable with a normal proper-motion distribution.

3.2. Radial Velocity

For the radial-velocity measurement, we first obtained well-calibrated wavelength solutions for our spectra. MAKEE performs an initial calibration of the wavelength using lamp spectra and then refines it by cross-correlating the night-sky lines for each observation and determining minor offsets. Both science objects and radial-velocity standards were reduced in the same fashion.

Each order of each star spectrum was then cross-correlated using the IRAF task FXCOR (Tonry & Davis 1979) with at least two other radial-velocity standards (HR6349, HR6970, or HR1283) which had been observed on the same night. We measure the radial velocity of the standards and, comparing to the canonical

Table 2
Proper Motions of Candidates

| Tycho (Name)	α(J2000) (hh:mm:ss.ss)	δ(J2000) (dd:mm:ss.ss)	μ_α (mas yr^{-1})	μ_δ	$\Delta\mu_\alpha$ (mas yr^{-1})	$\Delta\mu_\delta$	μ_l (mas yr^{-1})	μ_b	r ($''$)
B	0:25:19.97	64:08:17.1	−1.24	0.56	0.62	0.64	−1.17	0.68	4.86
A	0:25:19.73	64:08:19.8	−0.09	−0.89	1.17	0.90	−0.18	−0.88	6.21
A2	0:25:19.81	64:08:20.0	−0.71	−3.60	0.69	0.64	−1.07	−3.51	6.58
C	0:25:20.38	64:08:12.2	−0.21	−2.52	0.65	0.65	−0.46	−2.48	6.66
E	0:25:18.28	64:08:16.1	2.04	0.54	0.66	0.69	2.09	0.33	7.60
D	0:25:20.62	64:08:10.8	−1.12	−1.99	1.01	0.86	−1.32	−1.87	8.60
1	0:25:16.66	64:08:12.5	−2.27	−1.37	1.60	1.15	−2.40	−1.14	18.00
F	0:25:17.09	64:08:30.9	−4.41	0.20	0.70	0.71	−4.37	0.65	22.69
J	0:25:15.08	64:08:05.9	−2.40	−0.25	0.62	0.62	−2.42	−0.00	29.44
G	0:25:23.58	64:08:01.9	−2.50	−4.22	0.60	0.60	−2.91	−3.95	29.87
R	0:25:15.51	64:08:35.4	0.28	0.24	0.89	0.80	0.30	0.21	33.23
N	0:25:14.73	64:08:28.1	1.18	0.89	0.86	0.98	1.27	0.77	33.66
U	0:25:19.24	64:07:37.9	0.01	−3.04	0.73	0.75	−0.30	−3.03	36.06
Q	0:25:14.81	64:08:34.2	1.45	3.07	0.64	0.72	1.75	2.91	36.19
T	0:25:14.58	64:07:55.0	−3.85	0.52	0.72	0.62	−3.77	0.91	36.78
K	0:25:23.89	64:08:39.3	0.18	0.17	0.73	0.69	0.20	0.15	38.73
L	0:25:24.30	64:08:40.5	0.16	−0.44	0.75	0.82	0.11	−0.45	41.59
S	0:25:13.78	64:08:34.4	4.16	0.58	0.83	0.84	4.20	0.15	42.09
2	0:25:22.44	64:07:32.4	74.85	−4.43	0.82	0.83	74.05	−11.94	46.09
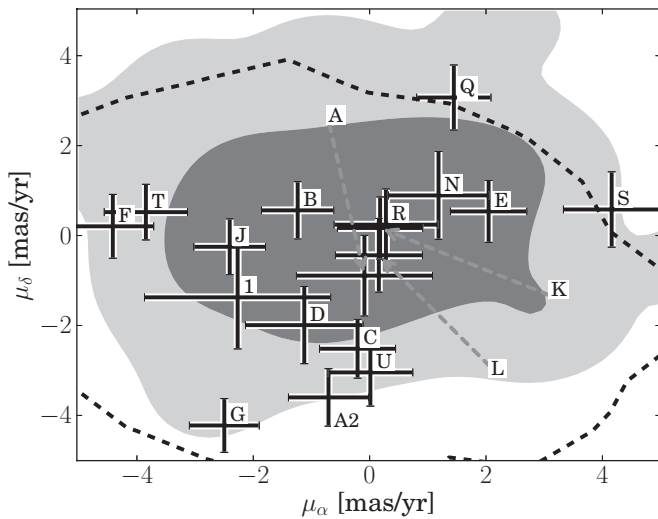
Figure 1. Contours display the distribution of proper motions (68% and 95% probability) for all stars measured toward the Tycho SNR, excluding the named stars. We show the location of the candidate stars and their uncertainties on top of this distribution. Tycho-2 (called HP-1 in WEK09) is not shown in this figure as it is an extreme outlier with $\mu_\alpha = 75$ mas yr^{-1} and $\mu_\delta = -4.4$ mas yr^{-1}; it is also at a large distance from the remnant's geometric center (46$''$). In addition, the dashed contour represents the 1σ level of the thick disk proper motion according to the Besançon model. Using the same Besançon model as a proxy, we estimate the contamination of the *HST* sample with foreground objects (less than 2 kpc) to be roughly 30%.

Table 3
Radial Velocities of Candidates

Tycho (Name)	Date (dd/mm/yy)	$v_{\rm helio}$ (dd:mm:ss.ss)	$v_{\rm LSR}$ (km s^{-1})	σ (km s^{-1})
Tycho-A	09/09/06	−36.79	−28.50	0.23
Tycho-B	09/09/06	−52.70	−44.41	∼2
Tycho-C	11/10/06	−58.78	−50.49	0.75
Tycho-D	11/10/06	−58.93	−50.64	0.78
Tycho-E[a]	11/10/06	−64.20	−55.91	0.27
Tycho-G	09/09/06	−87.12	−78.83	0.25
Tycho-G	11/10/06	−87.51	−79.22	0.78

Note. [a] There seems to be a discrepancy between RP04 and this work (measurement by RP04 $v_{\rm LSR}$ −26 km s^{-1}), which might be a possible hint of a binary system.

radial-velocity measurement of all orders added in quadrature to the error of the radial-velocity standards.

In Figure 2, we compare the radial velocity of our sample stars to the radial velocities of stars in the direction of Tycho's SNR using the Besançon model (Robin et al. 2003). The distances as well as their uncertainties are taken from Section 3.6. The candidates' radial velocities are all typical for their distances. Finally, we note that the measurement of Tycho-G is consistent with the results of WEK09 and GH09.

3.3. Rotational Velocity

We have measured the projected rotational velocities ($v_{\rm rot}\sin i$) of all stars except Tycho-B in the fashion described by WEK09. We selected several unblended and strong (but not saturated) Fe I lines in the stellar spectra and averaged them after shifting to the same wavelength and scaling to the same equivalent width (EW). This was done to improve the S/N for the faint stars as well as to provide consistency throughout all stars.

As a reference, we created three synthetic spectra for each star (one broadened only with the instrumental profile, the others with the instrumental profile and a $v_{\rm rot}\sin i$ of 10 and 13 km s^{-1}) with the 2010 version of MOOG (Sneden 1973),

values (Stefanik et al. 1999), we obtain a systematic error of ∼1 km s^{-1}, which is negligible compared to the measured velocities.

The radial velocity of Tycho-B was measured in the course of determining the stellar parameters of Tycho-B with the stellar parameter fitting package SFIT (Jeffery et al. 2001). The SFIT result consistently gives $v_{\rm helio} = -52$ km s^{-1} for different stellar parameters with an uncertainty of ∼2 km s^{-1}.

In Table 3, we list all of the radial velocities both in a heliocentric frame and a local standard of rest (LSR) frame. We will be referring to the heliocentric measurements henceforth. The listed uncertainty is the standard deviation of the

Figure 2. Contours indicating the 1σ, 2σ, and 3σ levels of the distance and radial velocity using the Besançon Model (Robin et al. 2003) with $\sim 60{,}000$ stars in the direction of SN 1572 (only including stars with $10 < V < 20$ mag and with a metallicity of [Fe/H] > -1 for the filled contours and [Fe/H] > -0.2 for the dashed contours). We have overplotted our candidate stars with error bars. One should note that the uncertainties in distance are a marginalized approximation of the error; the proper error surfaces can be seen in Figure 12. The vertical gray shade illustrates the error range for the distance to SNR 1572.

Table 4
Stellar Parameters

Tycho	$T_{\rm eff}$ (K)	$\log g$ (dex)	ξ_t (km s^{-1})	[Fe/H] (dex)
A	4975	2.9	1.20	0.04
B	10722	4.13	2	−1.1
C	4950	2.9	2.14	−0.55
E	5825	3.4	1.82	−0.13
G	6025	4.0	1.24	−0.13

using our derived temperature, surface gravity, and metallicity. As input data to MOOG, we used the Castelli & Kurucz (2004) atmospheric models and a line list from Kurucz & Bell (1995). We then applied the same process of line selection and adding as for the lines in the observed spectra.

Figure 3 shows the comparison between the synthetic spectra with different rotational velocities and the observed spectra. It indicates that the stellar broadening (rotational, macroturbulence, etc.) is less than broadening due to the instrumental profile of 6 km s^{-1} for each star. We adopt 6 km s^{-1} as an upper limit to the rotation for all stars.

Due to its high temperature and rotation, we fit the rotational velocity for Tycho-B with the program SFIT (Jeffery et al. 2001, described in Section 3.4) as part of the overall fit for this star's stellar parameters. We find $v_{\rm rot} \sin i = 171^{+16}_{-33}$ km s^{-1}. While Tycho-B's rotation is very high compared to the other candidate stars, for stars of this temperature and surface gravity a high rotation is not unusual.

In summary, other than Tycho-B, none of the stars show rotation which is measurable at this resolution.

3.4. Stellar Parameters and Chemical Abundances

The stellar parameters are presented in Table 4 and were determined using a traditional spectroscopic approach. Due to its high temperature, we measure the stellar parameters for Tycho-B

by a direct comparison to models in a separate procedure described later in this subsection.

The first step in the spectroscopic analysis was to rectify the continuum. For each order, we fit the continuum by eye, using a low-order polynomial function within the CONTINUUM task in IRAF. To help identify continuum regions in the program stars, we made use of the Arcturus and solar spectra (Hinkle et al. 2000). Consideration of the moderate S/N was a concern. For example, at these values of the S/N, we were mindful of not fitting the continuum to the highest points since it is likely that these values are noise rather than true continuum regions.

Next, EWs for a set of Fe and Ni lines were measured using routines in IRAF. The log gf values for the Fe I lines were from the laboratory measurements by the Oxford group (e.g., Blackwell et al. 1979a, 1979b, 1980, 1986, 1995 and references therein) and the Fe II lines were from the measurements by Biemont et al. (1991). For Ni, the log gf values were taken from the compilation by Reddy et al. (2003, henceforth Reddy03) and Ramírez & Cohen (2002, henceforth RC02). While these EW measurement routines employ Gaussian fits in a semi-automated manner, we emphasize that all EWs were visually checked on at least two occasions. We also required that lines have an EW of at least 10 mÅ to avoid measuring noise and less than ~ 150 mÅ to avoid saturated lines with non-Gaussian profiles that may lie on the flat part of the curve of growth. Table 5 shows the EWs measured for the program stars. Missing values indicate that the line was not detected or that no reliable measurement could be obtained. In the following subsection, we consider in more detail the uncertainties that arise from continuum placement and EW errors.

We used the 2011 version (Sobeck et al. 2011) of the local thermodynamic equilibrium (LTE) stellar line analysis program MOOG (Sneden 1973) and LTE model atmospheres from the Castelli & Kurucz (2003) grid to derive an abundance for a given line. The effective temperature, $T_{\rm eff}$, was adjusted until the abundances from Fe I lines displayed no trend as a function
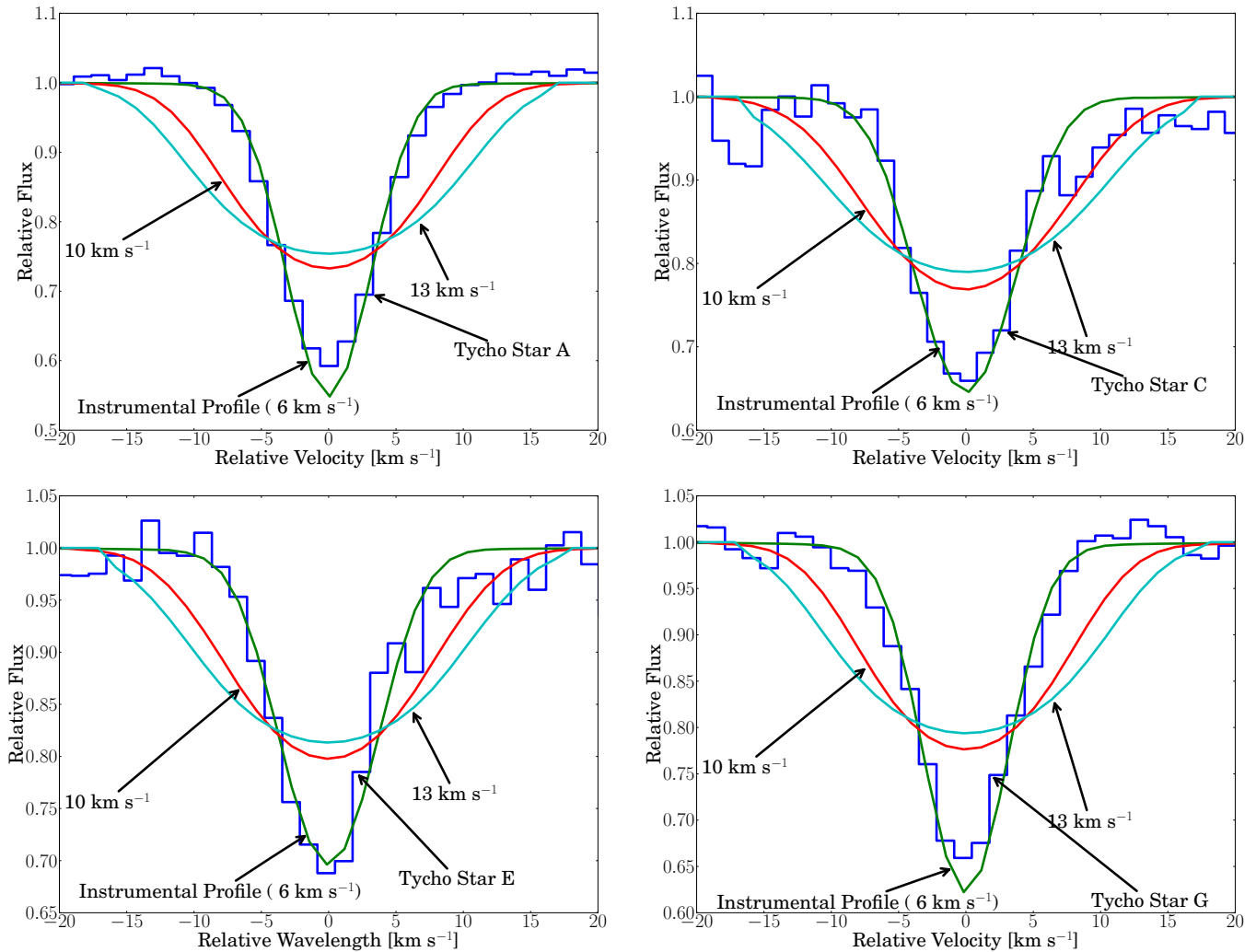
Figure 3. Combined (averaged) iron line profiles after normalization to the same EW, compared with synthetic line profiles created by MOOG. We convolved the synthetic lines first with a rotational kernel having three different values for rotation and then with the instrumental profile. All stars show rotation less than 6 km s^{-1}, which is equal to the instrumental profile at this resolution.

(A color version of this figure is available in the online journal.)

of lower excitation potential, χ. The surface gravity, log g, was adjusted until the abundances from the Fe I and Fe II lines were in agreement. The microturbulent velocity, ξ_t, was adjusted until there was no trend between the abundances from the Fe I lines and the reduced EW, log (EW/λ). This process was iterated until self-consistent stellar parameters were obtained for each star.

In our analysis, we explored stellar parameters at discrete values. For effective temperature, we considered values at every 25 K (e.g., 6000, 6025 K, etc.); for surface gravity, we considered values at every 0.05 dex (e.g., 4.00, 4.05 dex, etc.); and for ξ_t, we considered values at every 0.01 km s^{-1} (e.g., 1.70, 1.71 km s^{-1}, etc.). We assumed that excitation equilibrium was satisfied when the slope between log ϵ(Fe I) and lower excitation potential (χ) was $\leqslant 0.004$. We assumed that ionization equilibrium was achieved when log ϵ(Fe I) $-$ log ϵ(Fe II) $\leqslant$ 0.02 dex. The microturbulent velocity was set when the slope between log ϵ(Fe I) and reduced EW (log EW/λ) was $\leqslant 0.004$. We found a unique solution for all program stars. We estimate that the internal uncertainties are typically $T_{eff} \pm 100$ K, log $g \pm 0.3$ dex, and $\xi_t \pm 0.3$ km s^{-1}. For further details regarding the derivation of stellar parameters, see Yong et al. (2008).

The final iron measurements are the average of Fe I and Fe II, weighted by the number of lines measured for each species. We adopted the solar abundances of Asplund et al. (2009).

In addition, we measured element abundance ratios for Ni via EW analysis and Li (only for Tycho-G) via spectrum synthesis (see Figure 4). For the Li spectrum synthesis, we used the Bensby et al. (2005) line list in combination with MOOG and the Castelli & Kurucz (2003) model atmospheres. A non-LTE (NLTE) analysis (Lind et al. 2009) of the Li abundances (A(Li)$_{NLTE}$ = 2.45) yields nearly the same result as the LTE abundance (A(Li) = 2.46). Abundances are presented in Table 6. Tycho-B's abundances are not presented in the table as they were measured in a different fashion.

In summary, the inferred metallicities for all candidates show that the candidates are of roughly solar metallicity, with the exception of the metal-poor Tycho-C. The range of metallicities spanned by the program stars is compatible with membership in the thin disk. Based on metallicity alone, we do not regard any of the program stars to be unusually metal-poor or metal-rich. Additionally, we have compared the [Ni/Fe] abundance ratio to a well-calibrated set of F- and G-dwarf abundances (Bensby et al. 2005), which we calibrated to the solar abundances of

Table 5
Line List and Equivalent Width Measurements

Wavelength (Å)	Species	χ (eV)	log gf	Star A	Star C	Star E	Star G	Source
					EW (mÅ)			
(1)	(2)	(3)	(4)	(5)	(6)	(7)	(8)	(9)
4602.00	26.0	1.607	−3.154	114.8	. . .	. . .	. . .	Oxford
4733.59	26.0	1.484	−2.987	. . .	. . .	102.3	85.4	Oxford
4802.88	26.0	3.692	−1.531	91.0	96.0	. . .	64.8	Oxford
4848.88	26.0	2.277	−3.154	. . .	85.9	. . .	. . .	Oxford
4930.31	26.0	3.957	−1.264	. . .	. . .	. . .	57.8	Oxford
4962.57	26.0	4.175	−1.199	77.5	. . .	. . .	. . .	Oxford
5014.94	26.0	3.940	−0.320	. . .	. . .	. . .	106.8	Oxford
5044.21	26.0	2.849	−2.034	109.1	. . .	. . .	67.2	Oxford
5049.82	26.0	2.277	−1.372	. . .	. . .	. . .	117.8	Oxford
5054.64	26.0	3.637	−1.938	70.8	. . .	. . .	30.4	Oxford
5083.34	26.0	0.957	−2.958	. . .	. . .	. . .	96.2	Oxford
5141.74	26.0	2.422	−2.001	123.9	. . .	. . .	85.4	Oxford
5151.91	26.0	1.010	−3.322	. . .	. . .	. . .	85.0	Oxford
5166.28	26.0	0.000	−4.195	. . .	. . .	111.6	. . .	Oxford
5194.94	26.0	1.556	−2.090	. . .	. . .	. . .	113.8	Oxford
5198.71	26.0	2.221	−2.135	. . .	. . .	. . .	92.1	Oxford
5217.39	26.0	3.209	−1.179	. . .	. . .	123.7	81.9	Oxford
5223.19	26.0	3.632	−1.800	58.5	. . .	33.9	27.7	Oxford
5225.52	26.0	0.110	−4.789	. . .	. . .	82.3	65.6	Oxford
5242.49	26.0	3.632	−0.984	113.9	. . .	110.6	69.8	Oxford
5247.05	26.0	0.087	−4.946	. . .	. . .	76.6	55.5	Oxford
5250.21	26.0	0.121	−4.938	. . .	. . .	. . .	59.9	Oxford
5253.46	26.0	3.281	−1.630	. . .	. . .	. . .	62.4	Oxford
5412.80	26.0	4.431	−1.783	38.2	. . .	. . .	. . .	Oxford
5491.84	26.0	4.183	−2.253	36.9	. . .	. . .	. . .	Oxford
5497.52	26.0	1.010	−2.849	. . .	. . .	129.3	102.1	Oxford
5501.46	26.0	0.957	−3.063	. . .	. . .	. . .	90.9	Oxford
5506.78	26.0	0.989	−2.797	. . .	. . .	. . .	95.7	Oxford
5525.54	26.0	4.227	−1.149	. . .	. . .	. . .	38.4	Oxford
5569.62	26.0	3.414	−0.544	. . .	. . .	123.1	113.4	Oxford
5586.76	26.0	3.366	−0.161	. . .	. . .	142.8	. . .	Oxford
5600.23	26.0	4.257	−1.486	. . .	. . .	. . .	44.2	Oxford
5618.63	26.0	4.206	−1.292	80.1	. . .	. . .	43.3	Oxford
5661.35	26.0	4.281	−1.822	48.2	. . .	. . .	18.0	Oxford
5662.51	26.0	4.175	−0.590	115.6	. . .	79.1	69.5	Oxford
5701.55	26.0	2.557	−2.216	. . .	. . .	104.7	. . .	Oxford
5705.47	26.0	4.298	−1.421	78.9	69.5	. . .	. . .	Oxford
5741.85	26.0	4.253	−1.689	58.0	. . .	. . .	. . .	Oxford
5753.12	26.0	4.257	−0.705	. . .	. . .	. . .	52.0	Oxford
5775.08	26.0	4.217	−1.314	82.3	73.0	. . .	34.5	Oxford
5778.45	26.0	2.586	−3.481	55.5	58.5	. . .	. . .	Oxford
5816.37	26.0	4.545	−0.618	. . .	. . .	. . .	66.5	Oxford
5855.09	26.0	4.604	−1.547	43.1	. . .	17.1	. . .	Oxford
5909.97	26.0	3.209	−2.643	. . .	44.9	. . .	36.5	Oxford
5916.25	26.0	2.452	−2.994	. . .	73.6	. . .	44.1	Oxford
5956.69	26.0	0.858	−4.608	107.2	101.5	59.7	34.9	Oxford
6012.21	26.0	2.221	−4.073	72.0	. . .	. . .	. . .	Oxford
6027.05	26.0	4.073	−1.106	100.3	79.9	. . .	63.3	Oxford
6065.48	26.0	2.607	−1.530	. . .	. . .	106.2	. . .	Oxford
6082.71	26.0	2.221	−3.573	. . .	61.6	. . .	. . .	Oxford
6120.24	26.0	0.914	−5.970	33.9	. . .	. . .	. . .	Oxford
6136.62	26.0	2.452	−1.400	. . .	. . .	145.6	. . .	Oxford
6136.99	26.0	2.196	−2.950	. . .	. . .	71.7	. . .	Oxford
6151.62	26.0	2.174	−3.299	91.4	81.8	33.7	36.6	Oxford
6165.36	26.0	4.140	−1.490	73.5	. . .	54.0	. . .	Oxford
6173.34	26.0	2.221	−2.880	115.1	. . .	. . .	52.8	Oxford
6180.20	26.0	2.725	−2.637	. . .	61.0	. . .	46.8	Oxford
6200.31	26.0	2.607	−2.437	. . .	109.6	. . .	66.6	Oxford
6219.28	26.0	2.196	−2.433	. . .	134.4	. . .	75.2	Oxford
6229.23	26.0	2.843	−2.846	82.3	. . .	61.5	. . .	Oxford
6230.73	26.0	2.557	−1.281	. . .	. . .	. . .	109.9	Oxford
6232.64	26.0	3.651	−1.283	114.5	129.1	106.6	65.3	Oxford
6246.32	26.0	3.600	−0.894	. . .	. . .	. . .	106.2	Oxford
6252.55	26.0	2.402	−1.687	. . .	. . .	. . .	100.8	Oxford

Table 5
(Continued)

Wavelength	Species	χ	$\log gf$	Star A	Star C	Star E	Star G	Source
(Å)		(eV)				EW (mÅ)		
(1)	(2)	(3)	(4)	(5)	(6)	(7)	(8)	(9)
6265.13	26.0	2.174	−2.550	. . .	. . .	. . .	75.0	Oxford
6270.22	26.0	2.856	−2.505	. . .	77.1	70.2	. . .	Oxford
6297.79	26.0	2.221	−2.740	120.6	115.1	93.5	61.7	Oxford
6301.50	26.0	3.651	−0.766	. . .	. . .	114.0	110.9	Oxford
6322.69	26.0	2.586	−2.426	120.9	119.1	. . .	. . .	Oxford
6335.33	26.0	2.196	−2.194	. . .	. . .	116.4	75.0	Oxford
6336.82	26.0	3.684	−0.916	. . .	. . .	. . .	69.1	Oxford
6344.15	26.0	2.431	−2.923	. . .	. . .	. . .	48.4	Oxford
6355.03	26.0	2.843	−2.403	. . .	101.7	93.4	64.4	Oxford
6393.60	26.0	2.431	−1.469	. . .	. . .	129.4	105.5	Oxford
6408.02	26.0	3.684	−1.066	. . .	127.1	87.4	80.7	Oxford
6411.65	26.0	3.651	−0.734	. . .	. . .	. . .	118.0	Oxford
6430.84	26.0	2.174	−2.006	. . .	. . .	135.0	102.5	Oxford
6481.87	26.0	2.277	−2.984	113.2	. . .	. . .	50.3	Oxford
6498.94	26.0	0.957	−4.687	. . .	121.1	. . .	35.3	Oxford
6574.23	26.0	0.989	−5.004	84.3	88.5	. . .	25.3	Oxford
6575.02	26.0	2.586	−2.727	108.2	115.3	. . .	51.0	Oxford
6592.91	26.0	2.725	−1.490	. . .	. . .	121.7	104.1	Oxford
6593.87	26.0	2.431	−2.422	. . .	. . .	99.1	75.4	Oxford
6609.11	26.0	2.557	−2.692	. . .	104.9	54.7	53.1	Oxford
6648.08	26.0	1.010	−5.918	48.2	. . .	. . .	. . .	Oxford
6677.99	26.0	2.690	−1.435	. . .	. . .	142.4	98.3	Oxford
6699.16	26.0	4.590	−2.170	24.6	15.8	. . .	. . .	Oxford
6739.52	26.0	1.556	−4.823	48.4	53.3	. . .	. . .	Oxford
6750.15	26.0	2.422	−2.621	120.0	96.6	70.2	60.0	Oxford
6752.70	26.0	4.635	−1.273	. . .	. . .	. . .	33.8	Oxford
6810.26	26.0	4.603	−1.003	73.7	. . .	. . .	37.5	Oxford
6837.02	26.0	4.590	−1.756	. . .	19.0	21.8	. . .	Oxford
7112.17	26.0	2.988	−3.044	86.4	48.9	40.7	. . .	Oxford
7223.66	26.0	3.015	−2.269	. . .	87.5	49.9	35.0	Oxford
7401.69	26.0	4.183	−1.664	. . .	38.8	30.4	. . .	Oxford
7710.36	26.0	4.217	−1.129	. . .	66.5	56.2	. . .	Oxford
7723.20	26.0	2.277	−3.617	. . .	86.2	37.3	. . .	Oxford
7912.86	26.0	0.858	−4.848	. . .	97.1	. . .	21.7	Oxford
7941.09	26.0	3.271	−2.331	76.6	42.5	. . .	23.9	Oxford
8075.15	26.0	0.914	−5.088	105.4	118.7	. . .	. . .	Oxford
4491.40	26.1	2.853	−2.684	. . .	. . .	106.6	. . .	Biemont93
4508.29	26.1	2.853	−2.312	104.1	106.2	. . .	108.0	Biemont93
4620.52	26.1	2.826	−3.079	75.7	. . .	. . .	69.7	Biemont93
4635.32	26.1	5.952	−1.275	. . .	. . .	48.1	23.9	Biemont93
4993.36	26.1	2.805	−3.485	58.4	. . .	. . .	. . .	Biemont93
5100.66	26.1	2.805	−4.135	. . .	. . .	. . .	42.1	Biemont93
5132.67	26.1	2.805	−3.901	41.5	. . .	. . .	. . .	Biemont93
5197.58	26.1	3.228	−2.233	101.2	. . .	. . .	86.8	Biemont93
5234.62	26.1	3.219	−2.151	105.4	. . .	. . .	93.4	Biemont93
5414.07	26.1	3.219	−3.750	45.8	. . .	. . .	. . .	Biemont93
5425.26	26.1	3.197	−3.372	58.1	63.6	. . .	. . .	Biemont93
5991.38	26.1	3.150	−3.557	. . .	30.0	54.4	23.5	Biemont93
6084.11	26.1	3.197	−3.808	37.3	. . .	. . .	. . .	Biemont93
6149.26	26.1	3.886	−2.724	48.1	. . .	53.2	38.2	Biemont93
6239.95	26.1	3.886	−3.439	. . .	. . .	. . .	25.8	Biemont93
6247.56	26.1	3.889	−2.329	60.4	. . .	74.7	68.7	Biemont93
6369.46	26.1	2.889	−4.253	38.5	28.2	41.7	24.1	Biemont93
6383.72	26.1	5.548	−2.271	. . .	. . .	. . .	12.4	Biemont93
6432.68	26.1	2.889	−3.708	62.8	39.0	. . .	. . .	Biemont93
6456.38	26.1	3.900	−2.075	. . .	. . .	. . .	75.7	Biemont93
6516.08	26.1	2.889	−3.450	. . .	. . .	. . .	54.7	Biemont93
7222.39	26.1	3.886	−3.295	. . .	. . .	. . .	20.0	Biemont93
7711.72	26.1	3.900	−2.543	68.6	. . .	85.7	58.9	Biemont93
5082.35	28.0	3.660	−0.590	87.3	. . .	69.2	65.5	Reddy03
5088.54	28.0	3.850	−1.040	53.2	. . .	. . .	30.2	Reddy03
5088.96	28.0	3.680	−1.240	53.4	. . .	. . .	. . .	Reddy03
5094.42	28.0	3.830	−1.070	48.3	. . .	. . .	. . .	Reddy03
5115.40	28.0	3.830	−0.280	89.1	. . .	. . .	. . .	Reddy03

Table 5
(Continued)

Wavelength	Species	χ	$\log gf$	Star A	Star C	Star E	Star G	Source
(Å)		(eV)			EW	(mÅ)		
(1)	(2)	(3)	(4)	(5)	(6)	(7)	(8)	(9)
5682.20	28.0	4.100	−0.470	75.5	. . .	. . .	. . .	RC02
5748.35	28.0	1.680	−3.260	74.7	62.2	. . .	. . .	RC02
5749.30	28.0	3.940	−1.990	17.1	. . .	. . .	. . .	RC02
5847.01	28.0	1.680	−3.410	64.9	39.5	. . .	. . .	Reddy03
6007.31	28.0	1.680	−3.340	66.0	37.9	. . .	. . .	RC02
6053.69	28.0	4.230	−1.070	40.5	. . .	. . .	. . .	RC02
6086.28	28.0	4.260	−0.520	61.9	. . .	. . .	34.0	RC02
6108.12	28.0	1.680	−2.440	111.8	94.6	. . .	53.6	RC02
6111.08	28.0	4.090	−0.810	60.9	22.5	. . .	. . .	Reddy03
6130.14	28.0	4.270	−0.940	43.9	. . .	. . .	. . .	Reddy03
6175.37	28.0	4.090	−0.550	69.6	55.7	. . .	46.8	Reddy03
6176.82	28.0	4.090	−0.260	85.8	57.4	56.7	57.4	Reddy03
6177.25	28.0	1.830	−3.510	50.3	. . .	. . .	. . .	Reddy03
6186.71	28.0	4.100	−0.970	52.7	. . .	. . .	21.6	RC02
6204.61	28.0	4.090	−1.110	46.2	. . .	. . .	. . .	Reddy03
6322.17	28.0	4.150	−1.170	39.5	. . .	. . .	. . .	RC02
6370.35	28.0	3.540	−1.940	38.4	. . .	. . .	. . .	RC02
6378.26	28.0	4.150	−0.830	56.1	40.9	. . .	. . .	Reddy03
6482.80	28.0	1.930	−2.630	88.8	64.4	. . .	24.1	RC02
6598.60	28.0	4.230	−0.980	44.8	24.9	. . .	. . .	RC02
6635.12	28.0	4.420	−0.830	45.1	. . .	. . .	. . .	RC02
6643.64	28.0	1.680	−2.030	151.0	127.3	95.1	71.8	Reddy03
6767.77	28.0	1.830	−2.170	127.1	129.1	. . .	66.9	RC02
6772.32	28.0	3.660	−0.970	78.0	. . .	. . .	. . .	Reddy03
6842.04	28.0	3.660	−1.470	58.1	. . .	. . .	23.9	RC02
7030.01	28.0	3.540	−1.730	53.6	. . .	. . .	. . .	RC02
7122.20	28.0	3.540	0.050	146.4	120.8	. . .	. . .	RC02
7261.92	28.0	1.950	−2.700	. . .	. . .	. . .	38.1	RC02
7327.65	28.0	3.800	−1.770	35.1	. . .	. . .	13.3	RC02
7409.35	28.0	3.800	−0.100	. . .	83.6	. . .	. . .	RC02
7414.50	28.0	1.990	−2.570	. . .	83.6	48.0	40.4	RC02
7422.28	28.0	3.630	−0.130	139.5	101.4	87.4	. . .	RC02
7574.05	28.0	3.830	−0.580	91.2	39.5	. . .	41.8	RC02
7748.89	28.0	3.700	−0.380	117.7	85.7	95.7	70.3	Reddy03
7788.93	28.0	1.950	−2.420	. . .	123.4	82.8	. . .	RC02
7797.59	28.0	3.900	−0.350	106.4	84.0	81.1	61.7	Reddy03
7917.44	28.0	3.740	−1.500	. . .	. . .	. . .	14.8	RC02

Notes. Oxford = Blackwell et al. (1979a, 1979b, 1980, 1986, 1995).
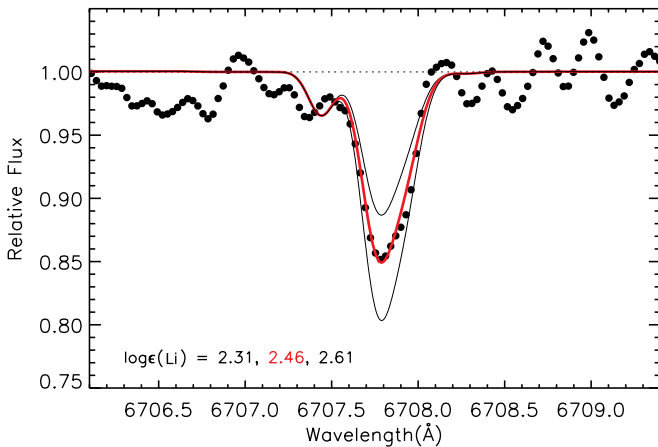
Figure 4. Observed spectra of Tycho-G centered around the Li λ6707 line. Synthetic spectra with different Li abundances are overplotted. The thick red line represents the Li abundance corresponding to the best-fitting value, and unsatisfactory fits (±0.15 dex) are plotted as thin black lines.
(A color version of this figure is available in the online journal.)

Asplund et al. (2009). Figure 5 shows that all program stars are consistent with stars of similar metallicity. We do note that Tycho-C is a marginal outlier (perhaps 1σ) with a low [Ni/Fe] abundance ratio, but we do not regard this to be significant. To avoid selection effects, we compared Tycho-C to a sample of giant stars (Luck & Heiter 2007), which gives a similar result as the comparison with Reddy et al. (2003).

Because Tycho-B has a temperature greater than 9000 K and is rapidly rotating, the process described above cannot be used to measure stellar parameters. Instead, we used the program SFIT to match the HIRES spectrum to a grid of model spectra. To determine the stellar parameters for Tycho-B, we have used a model grid with [Fe/H] = −1.0, 8000 < $T_{\rm eff}$ < 16,000 K, and 7 < $\log g$ < 2. This low metallicity is suggested by the very weak Ca II K line and Mg II lines, but it is hard to measure. We cannot measure helium directly in this spectrum and thus adopt N(He) = 0.1, as this is empirically a very common helium abundance in stars.

This analysis resulted in $T_{\rm eff}$ = 10,000$^{+400}_{-200}$ K, $\log g$ = 3.67 with slope $\partial \log g / \partial T_{\rm eff}$ = 0.27/500 K^{-1}, and rotational
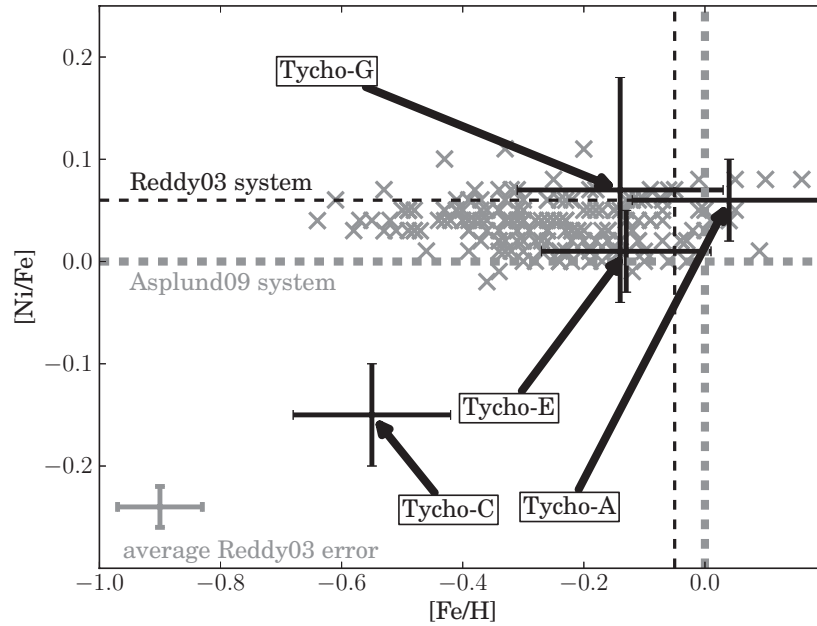
Figure 5. Background gray error bars are F- and G-dwarf abundances from Reddy et al. ([2003](#)). All candidate stars are consistent with that distribution. Tycho-C can be seen as an outlier, but it is a K-giant and its class is not represented in the underlying F- and G-dwarf distribution.

Table 6
Chemical Abundances and Error Estimates for the Program Stars

Species (1)	$\log \epsilon(X)_\odot$ (2)	$\log \epsilon(X)$ (3)	[X/H] (4)	[X/Fe] (5)	σ (6)	N_{lines} (7)	Δ_σ (8)	$\Delta_{T_{eff}}$ (9)	$\Delta_{\log g}$ (10)	Δ_ξ (11)	$\Delta_{[m/H]}$ (12)	$\Delta[X/H]$ (13)	$\Delta[X/Fe]$ (14)
						Star A							
Fe I	7.50	7.54	0.04	. . .	0.16	40	0.03	−0.08	−0.01	0.14	0.02	0.16	. . .
Fe II	7.50	7.54	0.04	. . .	0.15	14	0.04	0.07	−0.16	0.12	0.06	0.22	. . .
Ni I	6.22	6.33	0.10	0.06	0.08	37	0.01	−0.05	−0.04	0.11	0.03	0.13	0.04
						Star C							
Fe I	7.50	6.95	−0.55	. . .	0.23	36	0.04	−0.10	−0.02	0.07	0.01	0.13	. . .
Fe II	7.50	6.96	−0.54	. . .	0.27	5	0.12	0.05	−0.16	0.05	0.06	0.22	. . .
Ni I	6.22	5.52	−0.70	−0.15	0.21	20	0.05	−0.06	−0.04	0.07	0.03	0.10	0.05
						Star E							
Fe I	7.50	7.37	−0.13	. . .	0.22	40	0.03	−0.09	0.02	0.11	0.00	0.14	. . .
Fe II	7.50	7.38	−0.12	. . .	0.16	7	0.06	0.03	−0.14	0.08	0.03	0.18	. . .
Ni I	6.22	6.1	−0.12	0.01	0.17	8	0.06	−0.07	0.00	0.09	0.00	0.11	0.04
						Star G							
Fe I	7.50	7.37	−0.13	. . .	0.18	69	0.02	−0.09	0.03	0.09	0.01	0.13	. . .
Fe II	7.50	7.35	−0.15	. . .	0.18	16	0.05	0.01	−0.12	0.07	0.03	0.15	. . .
Ni I	6.22	6.16	−0.06	0.07	0.14	18	0.03	−0.07	0.01	0.05	0.01	0.09	0.04
Li	. . .	2.46	. . .	. . .	. . .	1	0.05[a]	−0.07	0.01	0.00	0.02	0.09	. . .

Note. [a] This represents the uncertainty in the fitting of the line.

velocity $v_{rot} \sin i = 171$ km s^{-1} with slope $\partial v_{rot} \sin i / \partial T_{eff} = -41/500$ km s^{-1} K^{-1}. From qualitative analysis this object seems metal-poor (e.g., in comparison with stars of similar stellar parameters but solar metallicity), but its high rotation and temperature make it hard to determine this parameter precisely. For the present, we assume [Fe/H] = −1.0 unless otherwise noted.

In addition, using the high-resolution spectrum, we measured the (EWs) of several lines predicted to be strong in the Vienna Atomic Line Database (Kupka et al. [2000](#)). The abundances were deduced from the EWs using a model atmosphere having $T_{eff} = 10,000$ K, $\log g = 3.67$, and [Fe/H] = −1.0 (see Table [7](#)).

One caveat regarding these abundances is the use of EWs from single lines with large rotational broadening, since the effect of blending with nearby weak lines cannot be taken into account. A second is that these abundances invariably rely on the strongest lines, which are precisely the most susceptible to departures from LTE. Nevertheless, they do confirm the earlier impression that the star is metal-poor, and justify the adoption of [Fe/H] = −1.0 ± 0.4.

As a second approach to determine the stellar parameters of Tycho-B, we used the low-resolution spectrum obtained with LRIS. The wavelength range of LRIS was chosen to be centered around the Balmer jump, as this feature is sensitive to the surface gravity (Bessell [2007](#)). We fitted the spectrum to a grid of

Table 7
Tycho-B Abundances

Ion Designation	λ (Å)	EW (Å)	ϵ (dex)	[X/H] (dex)	$\frac{\partial \epsilon}{\partial \log g}$	$\frac{\partial \epsilon}{\partial T_{\text{eff}}}$ (K^{-1})
Mg II	4481.13+4481.33	220 ± 15	$6.18 \pm .08$	-1.40	0.08	8×10^{-5}
Si II	6347.1	140 ± 5	$6.96 \pm .18$	-0.59	-0.02	1×10^{-4}
O I	7771.9+7774.2+7775.4	460 ± 30	$8.43 \pm .10$	-0.58	0.24	-4×10^{-5}
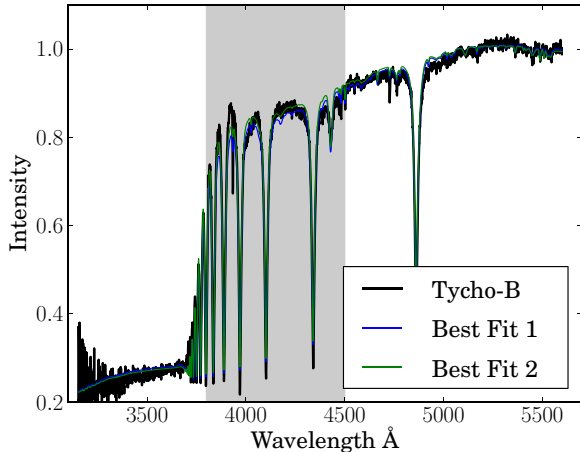
Figure 6. Normalized spectrum (intensity in F_λ) of Tycho-B with the fit that excluded the spectral region 3800–4500 Å (Best Fit 1) and the fit that included it (Best Fit 2). The region is marked with a gray shade.
(A color version of this figure is available in the online journal.)

model spectra (Munari et al. 2005) using a spectrum-fitting tool described below. The final grid we used covered $\log g$ from 3.5 to 4.5 in steps of 0.5 and effective temperature from 9000 to 12,000 K in steps of 500 K. In addition, we expanded the grid by reddening the spectra with the PYSYNPHOT[14] package. We also added diffuse interstellar bands (Beals & Blanchet 1937; Herbig 1966, 1967, 1975, 1995; Hibbins et al. 1994; Jenniskens & Desert 1994; Wilson 1958) to the synthetic spectra, scaled with reddening. The included $E(B - V)$ ranged from 0.5 to 1.3 mag in steps of 0.2. We assumed a rotation of 171 km s^{-1} in the grid (see Section 3.3).

We used χ^2 as a figure of merit in our fitting procedure. To find the best fit for Tycho-B, we used the MIGRAD algorithm provided by MINUIT and linearly interpolated between the grid points using LINEARNDINTERPOLATOR provided by the SCIPY package. The fit of Tycho-B results in $T_{\text{eff}} = 10{,}570$ K, $\log g = 4.05$, [Fe/H] $= -1.1$, and $E(B - V) = 0.85$ mag. The model fits the synthetic spectrum poorly in the wavelength region 3800–4280 Å (see Figure 6). The adopted mixing-length parameter in one-dimensional (1D) model atmospheres, used to construct the spectral grid, influences the fluxes in that region and affects the hydrogen line profiles. Heiter et al. (2002) and others show that a mixing length of 0.5, rather than 1.25 as used in the Kurucz/Munari grid, better fits the violet fluxes and the H line profiles. Spectra using a mixing-length parameter of 0.5 are brighter in the ultraviolet, and the Hδ, Hγ, and Hβ profiles give the same effective temperature as the Hα profiles. We have chosen, however, to fit the spectrum and ignore the problematic spectral region (3800–4280 Å) to avoid a systematic error. This yields $T_{\text{eff}} = 10{,}722$ K, $\log g = 4.13$, [Fe/H] $= -1.1$, and

$E(B - V) = 0.86$ mag. The differences are indicative of the size of systematic errors in the model fits. We adopt the fit excluding the problematic wavelength region in the subsequent analysis. Exploring the complex search space, we estimate the uncertainties to be $\Delta T_{\text{eff}} = 200$ K, $\Delta \log g = 0.3$, and Δ[Fe/H] $= 0.5$, and we note that the parameters are correlated.

3.5. Tycho-G: A Detailed Comparison with GH09

GH09 suggested that Tycho-G is a plausible donor star, with the primary evidence consisting of an unusually high Ni abundance and a high space velocity (radial velocity and proper motion). In this subsection, we focus on the Ni abundance, and we refer the reader to Sections 3.1, 3.2, and 4 on the proper motion and radial velocity.

The measured values are [Ni/Fe] $= 0.16 \pm 0.04$ and 0.07 ± 0.04 for GH09 and this study, respectively, from the same HIRES spectra. The magnitude of the difference is 0.09 dex, and it is significant at the $\sim 1.5\sigma$ level. While our [Ni/Fe] ratio in Tycho-G is lower than that measured by GH09, our value does not represent a substantial revision given the measurement uncertainties involved. Nevertheless, our [Ni/Fe] measurement and comparison with the literature do not support an unusually high Ni abundance, and we conclude that Tycho-G does not show any obvious chemical signature that one may seek to attribute to a supernova companion star. In order to identify the origin of the difference in [Ni/Fe] ratios, we now compare our stellar parameters and chemical abundances to those of GH09.

Both studies determined stellar parameters and chemical abundances in a similar manner, from a standard spectroscopic EW analysis using 1D LTE Kurucz model atmospheres and the MOOG stellar line analysis software. Our analysis employed more recent versions of both tools. The first test we can perform is to use the GH09 line list and stellar parameters but with our tools—namely, the 2011 version of MOOG (Sobeck et al. 2011; Sneden 1973) and the Castelli & Kurucz (2003) model atmospheres. Adopting this approach, we obtain $\log \epsilon$(Fe I) $= 7.38$ ($\sigma = 0.13$), $\log \epsilon$(Fe II) $= 7.42$ ($\sigma = 0.10$), and $\log \epsilon$(Ni I) $= 6.33$ ($\sigma = 0.19$). These values are in very good agreement with those of GH09, who obtained $\log \epsilon$(Fe I) $= 7.42$ ($\sigma = 0.12$), $\log \epsilon$(Fe II) $= 7.42$ ($\sigma = 0.10$), and $\log \epsilon$(Ni I) $= 6.36$ ($\sigma = 0.19$). Thus, we argue that any abundance differences (for Fe and Ni) between the two studies, exceeding the ~ 0.04 dex level, cannot be attributed to differences in the model-atmosphere grid and/or line-analysis software.

Our stellar parameters ($T_{\text{eff}} = 6000 \pm 100$ K, $\log g = 4.00 \pm 0.30$, [Fe/H] $= -0.13 \pm 0.13$) are in good agreement with those of GH09 ($T_{\text{eff}} = 5900 \pm 100$ K, $\log g = 3.85 \pm 0.30$, [Fe/H] $= -0.05 \pm 0.09$). The second test we can perform is to determine chemical abundances using (1) the GH09 stellar parameters but with our line list and (2) our stellar parameters and line list. On comparing case (2) minus case (1), we find $\Delta \log \epsilon$(Fe I) $= 0.10$, $\Delta \log \epsilon$(Fe II) $= 0.02$, and $\Delta \log \epsilon$(Ni I) $= 0.08$. Adopting the same solar abundances and method for

---

[14] The PYSYNPHOT package is a product of the Space Telescope Science Institute, which is operated by AURA for NASA.

Table 8
Comparison of Ni Measurement

Species (1)	$\log \epsilon(X)$ (2)	$[X/H]^a$ (3)	σ
	This work		
Fe I	7.37	−0.13	0.18
Fe II	7.35	−0.15	0.18
Ni I	6.16	−0.06	0.14
	Measurements from GH09		
Fe I	7.42	−0.08	0.10
Fe II	7.42	−0.08	0.12
Ni I	6.36	0.16	0.19
	This work using GH09's line list and stellar parameters		
Fe I	7.38	−0.12	0.13
Fe II	7.42	−0.08	0.10
Ni I	6.33	0.11	0.19
	This work using GH09's line list and this work's stellar parameters		
Fe I	7.42	−0.08	0.12
Fe II	7.42	−0.08	0.10
Ni I	6.36	0.14	0.19

Note. [a] Using solar values from Asplund et al. (2009).

determining the average [Fe/H] value (average of Fe I and Fe II weighted by the number of lines) as in the present study, we find Δ[Ni/Fe] = 0.00. We argue that while there are abundance differences for $\log \epsilon(X)$ at the ∼0.10 dex level, the [Ni/Fe] ratio remains unchanged, and therefore any differences in the [Ni/Fe] ratio between the two studies cannot be attributed to differences in the adopted stellar parameters.

The solar abundances for Fe and Ni differ between the two studies. GH09 adopt 7.47 and 6.25 for Fe and Ni, respectively, while we use 7.50 and 6.22 (from Asplund et al. 2009). Had we used the GH09 solar abundances, we would have obtained a ratio [Ni/Fe] = 0.01. Therefore, the different solar abundances adopted by the two studies only serve to decrease the discrepancy in the [Ni/Fe] ratio—that is, any difference in [Ni/Fe] cannot be attributed to the solar abundances.

The next series of comparisons we can perform concerns the line lists. We measured Fe and Ni abundances using the GH09 line list but with our stellar parameters and find $\log \epsilon(\mathrm{Fe\,I})$ = 7.42 (σ = 0.12), $\log \epsilon(\mathrm{Fe\,II})$ = 7.42 (σ = 0.10), and $\log \epsilon(\mathrm{Ni\,I})$ = 6.36 (σ = 0.19). Table 8 gives a comparison of all tests performed.

Adopting the same approach as before, regarding the solar abundances and metallicity, yields a ratio [Ni/Fe] = 0.22, a value that exceeds both our measurement and that of GH09. We therefore speculate that the difference in [Ni/Fe] between the two studies is driven primarily by differences in the line list. In particular, we note that while the Fe I and Fe II abundances are in fair agreement with our value and GH09, it is the Ni abundance, $\log \epsilon(\mathrm{Ni})$, that shows a large difference between the two studies: 6.16 ± 0.09 and 6.33 ± 0.10 for this study and GH09, respectively. Although the magnitude of this difference may appear large, 0.17 dex, it is significant only at the ∼1.3σ level.

On comparing the line lists between the two studies, we find three, two, and eight lines in common for Fe I, Fe II, and Ni, respectively. For these three species, the $\log gf$ values are on the same scale with differences (this study minus GH09) of −0.04 (σ = 0.07), −0.03 (σ = 0.04), and −0.01 (σ = 0.03) for
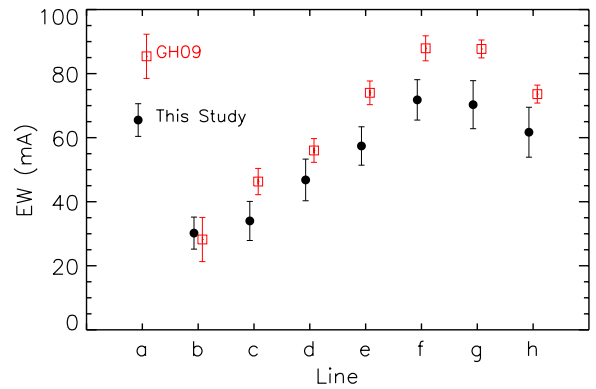
Figure 7. EWs for the eight Ni lines in common between GH09 (open red squares) and this study (filled black circles) for Tycho-G. Lines (a–h) are 5082.35 Å, 5088.54 Å, 6086.28 Å, 6175.37 Å, 6176.82 Å, 6643.64 Å, 7748.89 Å, and 7797.59 Å, respectively.

(A color version of this figure is available in the online journal.)

Fe I, Fe II, and Ni, respectively. Although the comparison sample is small, there is no clear evidence for any large systematic difference in $\log gf$ values that could explain the differing $\log \epsilon(\mathrm{Ni})$ or [Ni/Fe] values.

For the lines in common, our EWs are, on average, lower than those of GH09 by 5.7 mÅ (σ = 8.0 mÅ), 5.6 mÅ (σ = 5.4 mÅ), and 12.7 mÅ (σ = 6.9 mÅ) for Fe I, Fe II, and Ni, respectively. The most intriguing aspect of this comparison is that the Ni lines show the greatest discrepancy. In light of the EW differences for Fe I and Fe II, we may naively have expected the Ni EWs to show an offset of ∼6 mÅ rather than a 12.7 mÅ offset. Indeed, differences in the Ni EWs appear to be the primary reason for the difference in the derived Ni abundances between the two studies.

In Figure 7, we plot our EWs and the GH09 EWs, for the eight Ni lines in common. To estimate the uncertainties in our EWs, we use the Cayrel (1988) formula which considers the measurement uncertainty due to the line strength, S/N, and spectral resolution. Uncertainty in the continuum placement is *not* included in the Cayrel (1988) formula.

As noted in the previous subsection, we regard continuum placement as an additional source of uncertainty in the EW measurements. To quantify this uncertainty, we use the DAOSPEC program which fits the continuum and measures EWs (Stetson & Pancino 2008). Using DAOSPEC, we remeasure the Ni EWs using four different continuum fitting criteria: (1) adopting our continuum placement, and using a (2) third-order, (3) fifth-order, and (4) ninth-order polynomial to refit our continuum-rectified spectra. For a given line, we compute the dispersion in the EW measurements from the four different methods for continuum fitting and adopt this value as being representative of the EW uncertainties due to continuum rectification. We then add this value in quadrature to the uncertainty using the Cayrel (1988) value, noting that the latter value dominates the total EW error budget (see Table 9).

To establish whether these EW uncertainties are valid, we first identify the set of Ni EWs that produce our mean [Ni/Fe] ratio. That is, every line in this set of "ideal" EWs produces $\log \epsilon(\mathrm{Ni})$ = 6.16, i.e., [Ni/Fe] = 0.07. We then added to each of these ideal EWs a random number drawn from a normal distribution of width corresponding to our estimate of the EW uncertainty. We repeated this process for each Ni line, computed Ni abundances for this new set of lines, and measured the abundance dispersion. We repeated this process for 1000 new
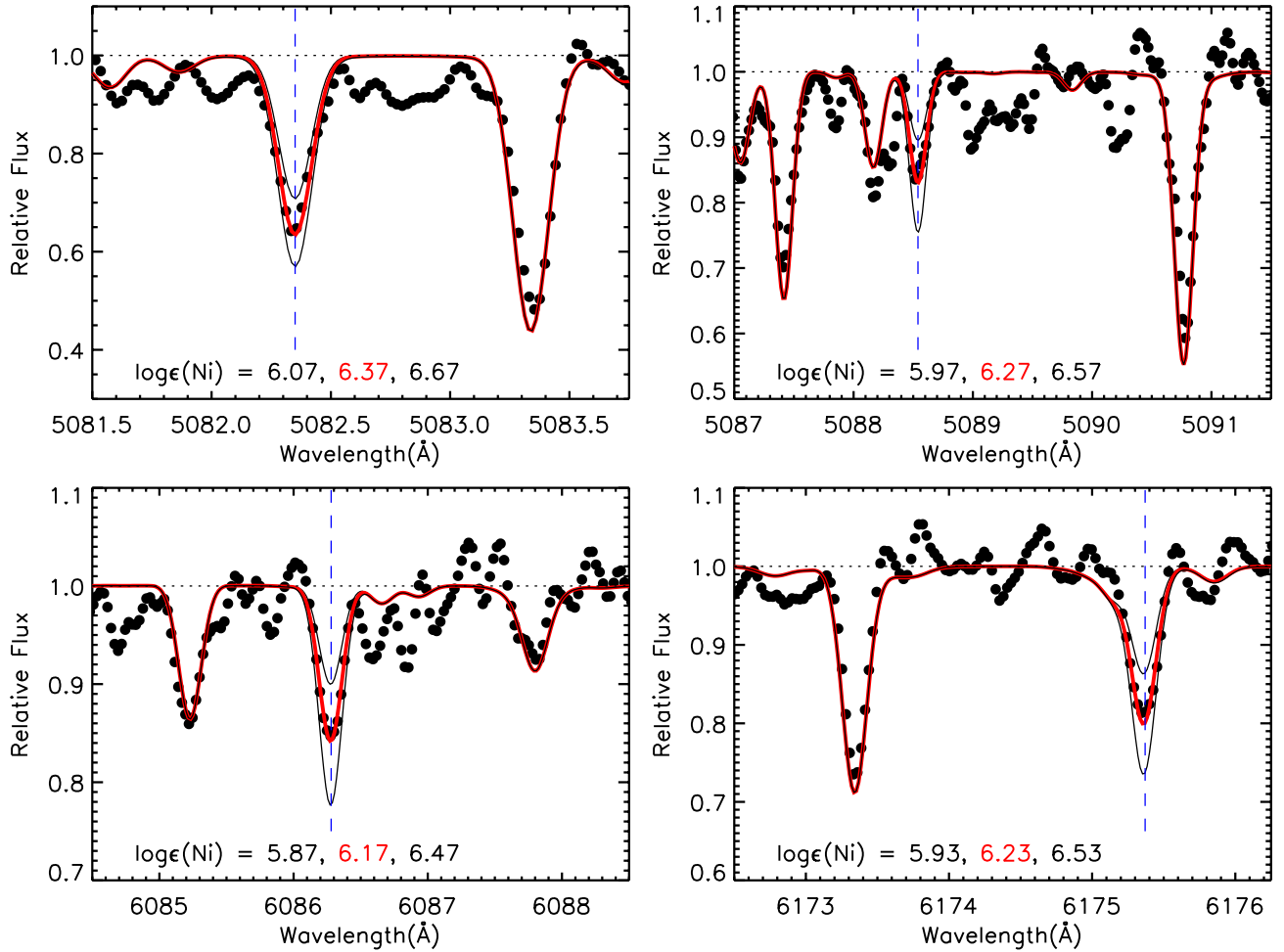
Figure 8. Observed spectra centered around five Ni lines in common with GH09 for Tycho-G. Synthetic spectra with different Ni abundances are overplotted. The thick red line represents the Ni abundance corresponding to the value derived from EW analysis, and unsatisfactory fits (±0.3 dex) are plotted as thin black lines.

(A color version of this figure is available in the online journal.)

Table 9
Equivalent Width Uncertainties for Ni in Star G

Wavelength (Å) (1)	EW (2)	σ_1[a] (3)	σ_2[b] (4)	σ_{Total}[c] (5)
5082.35	55.1	5.0	1.2	5.1
5088.54	25.7	5.0	0.8	5.0
6086.28	33.5	6.0	1.3	6.1
6108.12	58.1	5.8	1.1	5.9
6175.37	39.8	6.4	1.1	6.5
6176.82	54.4	6.0	1.0	6.0
6186.71	21.1	5.2	1.9	5.6
6482.80	37.6	6.0	0.7	6.0
6643.64	79.9	6.2	1.1	6.3
6767.77	66.9	6.8	2.4	7.2
6842.04	18.7	6.3	1.7	6.6
7261.92	35.6	6.7	1.3	6.9
7327.65	8.4	6.4	1.5	6.6
7414.50	40.9	7.0	0.2	7.0
7574.05	53.8	6.4	0.8	6.5
7748.89	71.3	7.4	0.7	7.5
7797.59	63.3	7.7	1.4	7.8
7917.44	16.8	7.5	0.4	7.5

Notes.
[a] This is the error from the Cayrel (1988) formula.
[b] This is the error due to continuum placement (see the text for details).
[c] This is the total error obtained by adding Columns 4 and 5 in quadrature.

random samples. The average dispersion in Ni abundance is 0.17 dex ($\sigma = 0.06$ dex), and this average value agrees well with our observed dispersion of 0.14 dex. Therefore, we are confident that our EW measurement uncertainties are realistic, since this Monte Carlo analysis verifies that these uncertainties reproduce our observed abundance dispersion.

An additional test is to measure EWs from our spectra for all Fe and Ni lines measured by GH09. As with our EWs, all lines were manually checked. For Fe I, we measured 27 lines and found a mean difference (this study minus GH09) of -1.9 mÅ $\pm$ 1.2 ($\sigma = 6.0$). For Fe II, we measured eight lines and found a mean difference of -4.6 mÅ $\pm$ 2.8 ($\sigma = 7.8$). For Ni, we measured 18 lines and found a mean difference of -8.7 mÅ $\pm$ 2.0 ($\sigma = 8.4$). This comparison confirms that our EWs are systematically lower than those of GH09 and that the Ni lines, in particular, show the largest discrepancy. Indeed, the average difference in Ni EWs is four times larger than the average difference in Fe I EWs. While continuum normalization could potentially explain these differences, these Ni lines lie in spectral regions similar to those of the Fe lines, so we would expect the differences in EWs for Fe and Ni to behave similarly.

We note in our line selection that we reject five, two, and four lines of Fe I, Fe II, and Ni (respectively) that were measured by GH09. These lines were in our opinion blended and/or in regions where the local continuum was poorly defined.
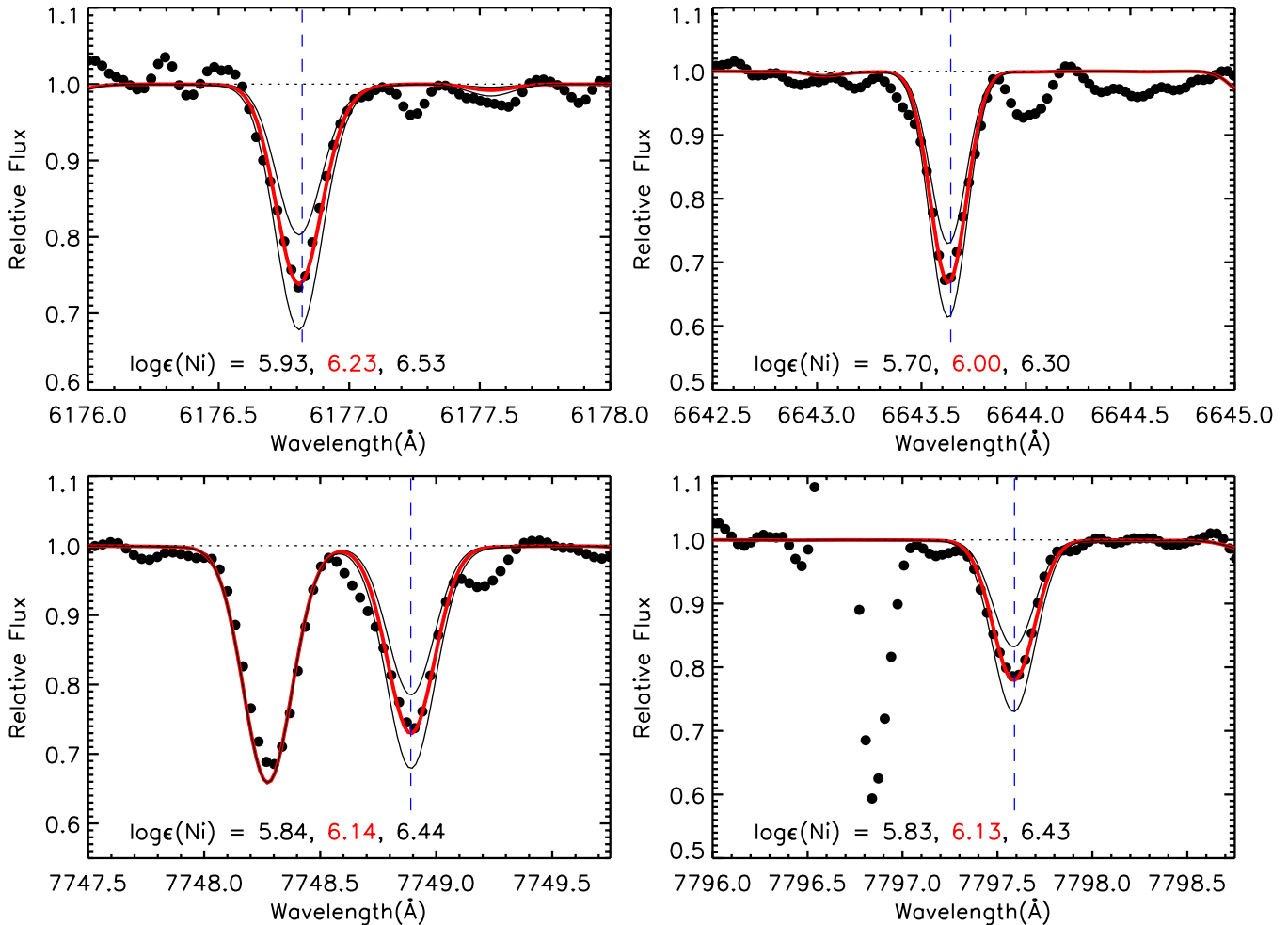
Figure 9. Same as Figure 8 but for the remaining four Ni lines in common with GH09 (the upper left line is also seen in the previous panel).

(A color version of this figure is available in the online journal.)

We return now to the eight Ni lines in common, noting that (1) for seven of the eight lines, our EWs are smaller than those of GH09; (2) for seven of the eight lines, the difference in EWs exceeds 1σ, and for all seven of these lines, the difference shows the same "sign"; and (3) for four of the eight lines, the difference in EWs exceeds 2σ, and for all four of these lines, the difference shows the same "sign."

Finally, for the eight Ni lines in common with GH09, we plot our normalized spectra along with spectrum syntheses (see Figures 8 and 9, and their corresponding continuum regions in Figures 10 and 11). The main points to take from these plots are the location of the continuum and how well the spectrum syntheses fit the lines for the abundances we measure. We note that our abundances were determined from EW analysis rather than spectrum synthesis. Nevertheless, had we relied solely upon spectrum synthesis, we would have obtained essentially identical results. A systematic increase in $\log \epsilon(\mathrm{Ni})$ of 0.17 dex or in [Ni/Fe] of 0.09 dex, as measured by GH09, is not supported by these spectrum syntheses.

The main conclusions we draw from this comparison are: (1) abundance differences between the two studies cannot be attributed to the different versions of model atmospheres and spectrum synthesis software; (2) the [Ni/Fe] ratio remains unchanged when using our line list but with either the GH09 stellar parameters or our stellar parameters; (3) differences in

[Ni/Fe] cannot be attributed to the adopted solar abundances; (4) although the set of lines in common between the two analyses is small, there are no large systematic differences in the $\log gf$ values that could explain the discrepancy in Ni abundances; (5) for Fe I and Fe II, our EWs are systematically lower than those of GH09 by $\sim$6 mÅ, and our Ni EWs are systematically lower by $\sim$12 mÅ; and (6) our EW uncertainties for Ni are consistent with the observed dispersion in the Ni abundance.

As noted above, while our measured [Ni/Fe] value does not represent a substantial revision of the GH09 value, our Ni abundance is not unusual with respect to field stars at the same metallicity.

Nevertheless, we welcome further analyses of this star, preferably conducted with higher-quality spectra.

3.6. Distances

To measure the distance to the candidate stars, we adopted colors and absolute magnitudes from isochrones by Pietrinferni et al. (2004). We used the MIGRAD algorithm (James & Roos 1975) to find close matches of the measured values to T_{eff}–$\log g$ isochrones by varying the age of the isochrone. Subsequently, we calculated $E(B - V)$ using the isochrone's color, and we extracted a mass from the isochrone. The results can be seen in Table 10. To estimate the uncertainties in all distances,
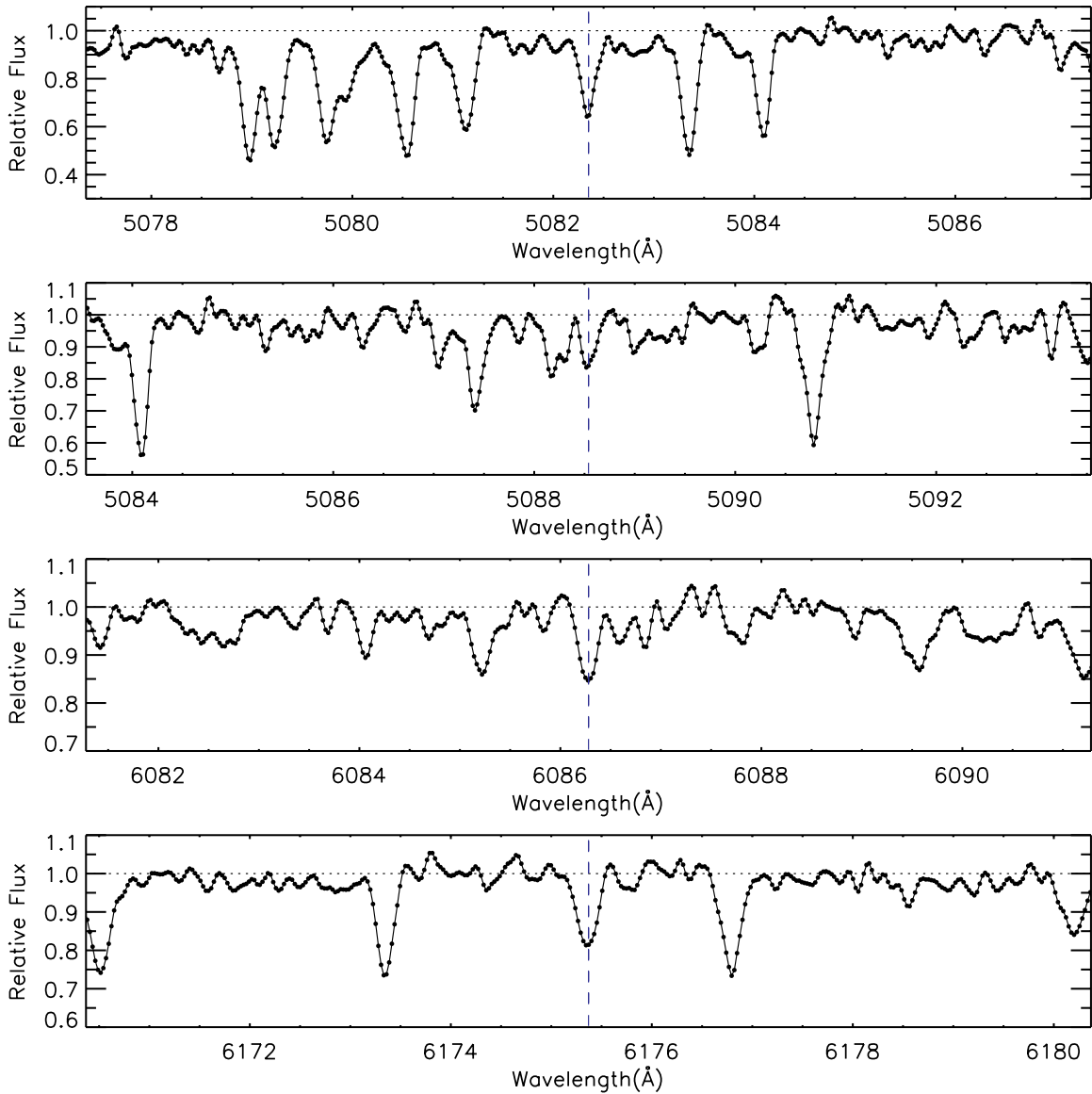
Figure 10. Overview of a larger continuum region for the lines measured in Figure 8.

Table 10
Distances, Ages, and Masses of Candidate Stars

Tycho (Name)	Mass ($M/M_\odot$)	σ_{Mass} ($M/M_\odot$)	Age (Gyr)	σ_{Age} (Gyr)	D (kpc)	σ_D (kpc)
Tycho-A	2.4	0.8	0.7	2.3	1.4	0.8
Tycho-B	1.8	0.4	0.8	0.3	1.8	0.8
Tycho-C	0.9	0.4	10.0	3.4	5.5	3.5
Tycho-E	1.7	0.4	1.4	1.1	11.2	7.5
Tycho-G	1.1	0.2	5.7	2.1	3.7	1.5

reddenings, and masses, we employed the Monte Carlo method with 10,000 samples of effective temperature, surface gravity, metallicity, B magnitude, and V magnitude (see Figure 12). Errors included in Table 10 are the standard deviations of the Monte Carlo sample. The data show that all stars are compatible with the distance of the remnant. This is not unexpected, as the uncertainties of the measurements in stellar parameters are relatively large.

4. DISCUSSION

In our sample of six stars, we find no star that shows characteristics which strongly indicate that it might be the donor star of SN 1572. On the other hand, it is difficult to absolutely rule out any particular star, if one is able to invoke improbable post-explosion evolutionary scenarios.

Tycho-A is a metal-rich giant, and it seems likely to be a foreground star. Its principal redeeming feature as a donor-star candidate is that it is located in the geometric center of the remnant and that it has a relatively low surface gravity. Tycho-A shows a very low spatial motion, which is consistent with a giant-donor-star scenario, although its lack of rotation is in conflict with a donor-star scenario. Taking all measurements into account, we regard Tycho-A as a very weak candidate (although a wind accretion scenario might still work).

Tycho-B's high temperature, position at the center of the remnant, high rotational velocity, and unusual chemical abundance make it the most unusual candidate in the remnant's center. Despite the a posteriori unlikely discovery of such a star in the remnant's center, Tycho-B's high rotational velocity coupled with

Figure 11. Overview of a larger continuum region for the lines measured in Figure 9.

its low spatial velocity seems to be in conflict with any viable donor-star scenario. These scenarios predict that the donor star will tidally couple to the white dwarf before explosion, causing the rotation and spatial motion to be correlated post-explosion (as discussed by WEK09). The large rotation seen in Tycho-B should be accompanied by a large spatial motion, which is ruled out by the observations presented here, a problem we are unable to reconcile with Tycho-B being the donor star. Tycho-B as a Lambda-Boötis star might explain some of the observed stellar parameters. Another explanation has been provided by Thompson & Gould (2012).

Tycho-C consists of two stars which are resolved only in *HST* images. It consists of a brighter bluer component ($B = 21.28$, $V = 19.38$, $R = 18.10$ mag; RP04) and a dimmer redder component ($B = 22.91$, $V = 20.53$, $R = 19.23$ mag; RP04). In our analysis, we find a consistent solution for the spectrum and infer that this is from the brighter bluer component. We find that Tycho-C is a metal-poor giant, probably located beyond the remnant. Tycho-C, similar to Tycho-A, might be compatible with a giant-donor-star scenario. Its lack of

rotation and its kinematics, however, make it an uncompelling candidate. The only information we have about the dimmer component is the proper motion, which is insignificant with $\mu_\alpha = 0.58 \pm 1.73$ mas yr^{-1}, $\mu_\delta = -0.29 \pm 1.21$ mas yr^{-1}.

Tycho-D is roughly a factor of 10 dimmer than the nearby star Tycho-C (separation $\approx 0\farcs6$). We could not measure reliable EWs of its spectrum, which has low S/N. Visual inspection of the star's spectral features shows it to be consistent with a cool star having low rotation. Its luminosity precludes it from being a relatively slowly rotating giant, and its slow rotation precludes it from being a subgiant or main-sequence donor star. All of this suggests that Tycho-D is an uncompelling donor candidate.

Tycho-E is the most distant star in this set (11.2 kpc), although large uncertainties in the distance remain. It seems to be similar to Tycho-G in temperature, but appears to have a lower surface gravity. It is located 7″ from the geometric center, but has no unusual stellar parameters or kinematics. GH09 have suggested this to be a double-lined binary, but we are unable to confirm this using Fourier cross-correlation techniques. Ihara et al. (2007) have looked at iron absorption lines in stellar spectra made by
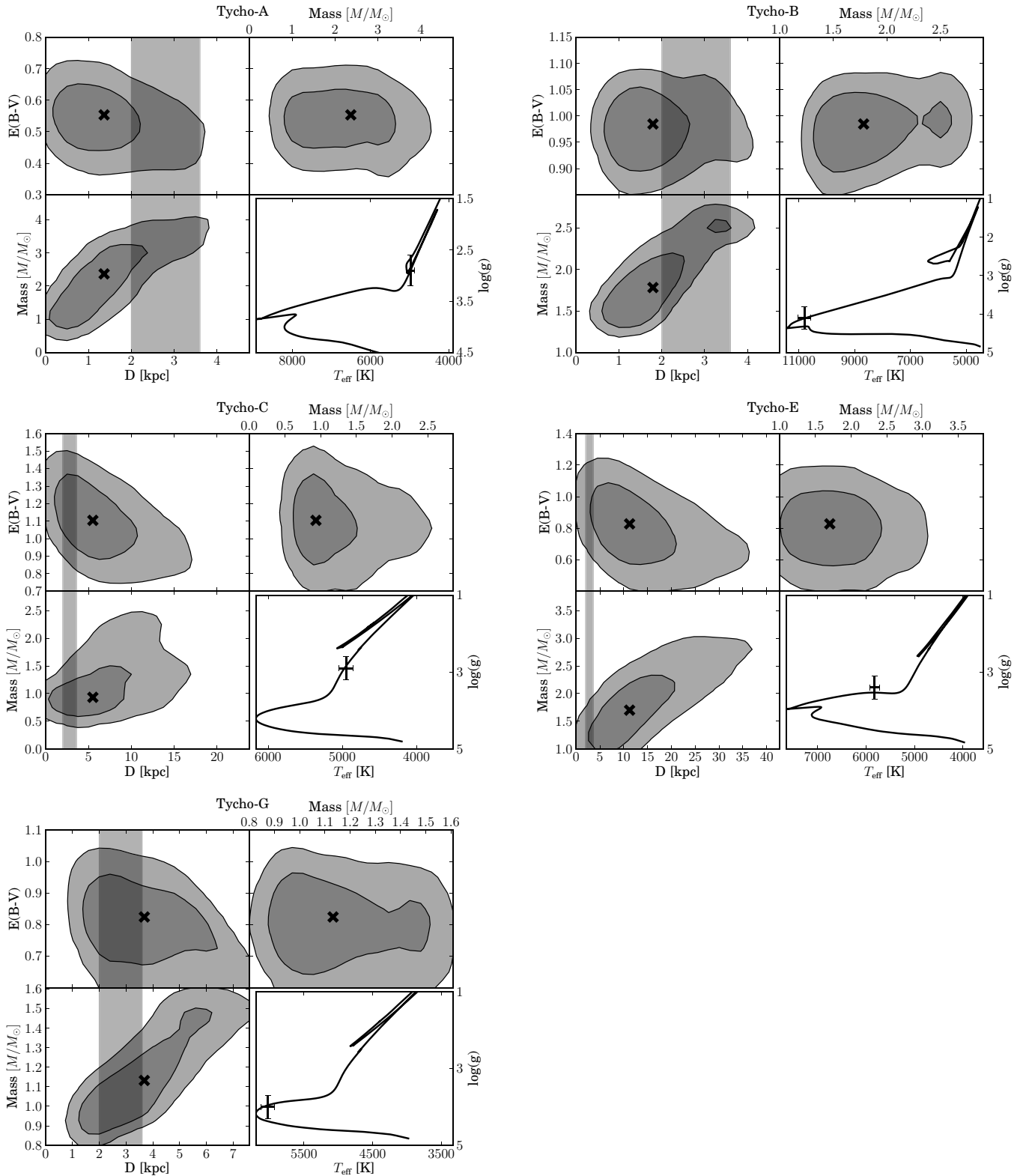
Figure 12. Error contours for distance, extinction, and mass of the candidates. In the distance plots, we indicate the distance range of SNR 1572 with a gray shade. The lower right shows the optimal isochrone (Pietrinferni et al. 2004) for the measured values of T_{eff} and log g.

the remnant and found Tycho-E to be unusual. They suggest that a star in the background would show blueshifted and redshifted iron lines, whereas a star inside the remnant would only show blueshifted iron lines, and a foreground star would not show any iron features from the remnant. Ihara et al. (2007) claim that Tycho-E only shows blueshifted lines, and thus suggest that it is inside the remnant. We believe, however, that Tycho-E is located far behind the remnant and suggest that a low column density on the receding side of the remnant could cause a lack of redshifted iron features. In summary, a lack of rotation, kinematic signatures, and an inconsistent distance make Tycho-E a very weak candidate.

Tycho-G is located $30''$ from the X-ray center, making it the most remote object from the center in this work (in the plane of the sky; for comparison a distance of $32''.6$ corresponds to $1000~\mathrm{km\,s^{-1}}$ over 433 yr at the distance of 2.8 kpc). This work confirms the radial velocity measured by GH09 and WEK09. Figure 2 shows the expected distribution of radial velocities from the Besançon model of Galactic dynamics. Tycho-G lies well within the expected range of radial velocity for stars with its stellar parameters and distance.

In addition, this work has analyzed the proper motion of stars around the center of SN 1572. Figure 1 shows Tycho-G to be a 2σ outlier, which implies that there should be about six stars in the *HST* sample sharing similar proper-motion features as Tycho-G; thus, its proper motion is by no means a unique trait. In particular, stars in the thick disk have motions entirely consistent with that of Tycho-G (see contours in Figure 1, and Figure 10 in GH09). Finally, the *HST* proper-motion measurements are challenging, and it is conceivable that there are systematic errors in our proper-motion measurements which are larger than our reported statistical errors. Such errors would tend to increase the chance of larger-than-actual proper-motion measurements. Taken in total, while Tycho-G may have an unusual proper motion, the significance of this motion, even if current measurements are exactly correct, is not exceptional.

As described, the kinematic features of a donor star might easily be lost in the kinematic noise of the Galaxy. WEK09 recommend using post-explosion stellar rotation as an additional possible feature for a donor star. This work suggests that Tycho-G has a rotation below the instrumental profile of $6~\mathrm{km\,s^{-1}}$, much less than expected for a donor star (for an estimate, see Kerzendorf et al. 2009). Recently, Pan et al. (2012a, 2012b) suggested that taking only tidal coupling into account could overestimate the rotation. However, all of their models (see Table 3 of Pan et al. 2012a) having a relatively low rotation rate are too luminous and too large to be consistent with Tycho-G. In fact, none of their calculated models can satisfy the constraints of the measured $\log g$ and the upper limit on v_{rot} simultaneously.

We find Tycho-G to be a subgiant/main-sequence star with roughly solar temperature and metallicity. GH09 measure a nickel enhancement, which they believe to originate in the contamination from the ejecta. We have conducted a detailed comparison with GH09's measurement in Section 3.5 and do not find Tycho-G to be an outlier as suggested by GH09, but rather consistent with other stars of similar metallicity. In addition, our Li measurement is in agreement with that of GH09 (see Table 6). In contrast to the GH09 interpretation, this Li abundance is consistent with that of stars of similar parameters (Baumann et al. 2010). Finally, we have measured the distance to Tycho-G, showing it to be consistent with a background star. In addition, the radial-velocity signature matches that of background stars (see Figure 2).

In summary, while Tycho-G may have unusual kinematics as indicated by its proper motion, the significance of this motion is not compelling when compared to a large sample of similar stars in the direction of the Tycho remnant. Furthermore, such a kinematic signature, if it were related to the binary orbital velocity, might predict rotation for Tycho-G which we do not observe (modulo the caveats from WEK09 and Pan et al. 2012b). All of the above evidence makes Tycho-G consistent with a background thick-disk interloper.

5. CONCLUSION

This work did not detect an unambiguously identifiable donor-star candidate to Tycho's SN 1572. Although Tycho-B shows some unusual features, there currently remains no convincing explanation for all of its parameters which can be attributed to the donor-star scenario. We believe that our results provide evidence that the Tycho SNR does not have a main-sequence, subgiant, or red giant donor star. Some other possibilities remain. In the spin-down scenario, the companion star can become a helium white dwarf from a red giant donor, or a very low-mass main-sequence star from a more massive main-sequence star. Such a compact companion can escape detection (Di Stefano et al. 2011; Justham 2011; Hachisu et al. 2012a, 2012b). Another scenario is a helium donor, such as the so-called sub-Chandrasekhar mass explosions discussed by Livne & Arnett (1995) and Sim et al. (2010). These progenitor systems might leave a very faint and fast-moving helium star, or no remnant at all (R. Pakmor 2012, private communication). Such a progenitor would probably evade detection and would likely not leave traces, such as circumstellar interaction with the remnant or early light-curve anomalies (Kasen 2010). Deep multi-epoch wide-field optical images should catch any such star speeding away from the remnant's center, but observations of this kind have not yet been taken. Finally, a double-degenerate progenitor, in most cases, does not leave a compact remnant, and is consistent with our finding no donor star in SNR 1572.

SN 1006 and SN 1604 (Kepler's SN) are two other SN Ia remnants in the Milky Way. SN 1006 is far from the Galactic plane and shows no signs of circumstellar interaction. Kerzendorf et al. (2012) have studied this remnant and have not found any unusual star that can be explained with a donor-star scenario (consistent with this work). SNR 1604, while far from the Galactic plane, shows circumstellar interaction with its remnant and has all the indications of what might be expected from an SD-scenario with an asymptotic giant branch donor (Chiotellis et al. 2012). Observations of these remnants will better establish if there is a continued pattern to the unusual stars in SN Ia remnant centers, or whether the lack of viable donor stars persists in multiple systems.

REFERENCES

Anderson, J., & King, I. R. 2006, PSFs, Photometry, and Astronomy for the ACS/WFC, Tech. Rep.
Asplund, M., Grevesse, N., Sauval, A. J., & Scott, P. 2009, ARA&A, 47, 481
Badenes, C., Borkowski, K. J., Hughes, J. P., Hwang, U., & Bravo, E. 2006, ApJ, 645, 1373
Baumann, P., Ramírez, I., Meléndez, J., Asplund, M., & Lind, K. 2010, A&A, 519, A87
Beals, C. S., & Blanchet, G. H. 1937, PASP, 49, 224
Bensby, T., Feltzing, S., Lundström, I., & Ilyin, I. 2005, A&A, 433, 185
Bessell, M. S. 2007, PASP, 119, 605
Bianco, F. B., Howell, D. A., Sullivan, M., et al. 2011, ApJ, 741, 20
Biemont, E., Baudoux, M., Kurucz, R. L., Ansbacher, W., & Pinnington, E. H. 1991, A&A, 249, 539
Blackwell, D. E., Booth, A. J., Haddock, D. J., Petford, A. D., & Leggett, S. K. 1986, MNRAS, 220, 549
Blackwell, D. E., Ibbetson, P. A., Petford, A. D., & Shallis, M. J. 1979a, MNRAS, 186, 633
Blackwell, D. E., Lynas-Gray, A. E., & Smith, G. 1995, A&A, 296, 217
Blackwell, D. E., Petford, A. D., & Shallis, M. J. 1979b, MNRAS, 186, 657
Blackwell, D. E., Petford, A. D., Shallis, M. J., & Simmons, G. J. 1980, MNRAS, 191, 445
Bloom, J. S., Kasen, D., Shen, K. J., et al. 2012, ApJL, 744, L17
Brown, P. J., Dawson, K. S., de Pasquale, M., et al. 2012, ApJ, 753, 22
Castelli, F., & Kurucz, R. L. 2003, in IAU Symp. 210, Modelling of Stellar Atmospheres, ed. N. Piskunov, W. W. Weiss, & D. F. Gray (San Francisco, CA: ASP), 20
Castelli, F., & Kurucz, R. L. 2004, arXiv Astrophysics e-prints
Cayrel, R. 1988, in IAU Symp. 132, The Impact of Very High S/N Spectroscopy on Stellar Physics, ed. G. Cayrel de Strobel & M. Spite (Dordrecht: Kluwer), 345
Chiotellis, A., Schure, K. M., & Vink, J. 2012, A&A, 537, A139
Chomiuk, L., Soderberg, A. M., Moe, M., et al. 2012, ApJ, 750, 164
Dan, M., Rosswog, S., Guillochon, J., & Ramirez-Ruiz, E. 2011, ApJ, 737, 89
Di Stefano, R., Voss, R., & Claeys, J. S. W. 2011, ApJL, 738, L1
Filippenko, A. V. 1997, ARA&A, 35, 309
Fink, M., Röpke, F. K., Hillebrandt, W., et al. 2010, A&A, 514, A53
Foley, R. J., Papenkova, M. S., Swift, B. J., et al. 2003, PASP, 115, 1220
Foley, R. J., Simon, J. D., Burns, C. R., et al. 2012, ApJ, 752, 101
Ganeshalingam, M., Li, W., & Filippenko, A. V. 2011, MNRAS, 416, 2607
González Hernández, J. I., Ruiz-Lapuente, P., Filippenko, A. V., et al. 2009, ApJ, 691, 1
Hachisu, I., Kato, M., & Nomoto, K. 2012a, ApJL, 756, L4
Hachisu, I., Kato, M., Saio, H., & Nomoto, K. 2012b, ApJ, 744, 69
Han, Z. 2008, ApJL, 677, L109
Hayden, B. T., Garnavich, P. M., Kasen, D., et al. 2010, ApJ, 722, 1691
Heiter, U., Kupka, F., van't Veer-Menneret, C., et al. 2002, A&A, 392, 619
Herbig, G. H. 1966, ZA, 64, 512
Herbig, G. H. 1967, in IAU Symp. 31, Radio Astronomy and the Galactic System, ed. H. van Woerden (London: Academic), 85
Herbig, G. H. 1975, ApJ, 196, 129
Herbig, G. H. 1995, ARA&A, 33, 19
Hibbins, R. E., Miles, J. R., Sarre, P. J., & Herbig, G. H. 1994, in The Diffuse Interstellar Bands, ed. A. G. G. M. Tielens (31
Hinkle, K., Wallace, L., Harmer, D., Ayres, T., & Valenti, J. 2000, in the 24th Meeting of the IAU, Joint Discussion, Vol. 1, High Resolution IR, Visible, and UV Spectroscopy of the Sun and Arcturus, ed. H. Rickman (Manchester: IAU)
Horesh, A., Kulkarni, S. R., Fox, D. B., et al. 2012, ApJ, 746, 21
Horne, K. 1986, PASP, 98, 609

Hughes, J. P. 2000, ApJL, 545, L53
Ihara, Y., Ozaki, J., Doi, M., et al. 2007, PASJ, 59, 811
James, F., & Roos, M. 1975, CoPhC, 10, 343
Jeffery, C. S., Woolf, V. M., & Pollacco, D. L. 2001, A&A, 376, 497
Jenniskens, P., & Desert, F. 1994, A&AS, 106, 39
Justham, S. 2011, ApJL, 730, L34
Kasen, D. 2010, ApJ, 708, 1025
Kerzendorf, W. E., Schmidt, B. P., Asplund, M., et al. 2009, ApJ, 701, 1665
Kerzendorf, W. E., Schmidt, B. P., Laird, J. B., Posiadlowski, P., & Bessell, M. S. 2012, ApJ, 759, 7
Krause, O., Tanaka, M., Usuda, T., et al. 2008, Natur, 456, 617
Kupka, F. G., Ryabchikova, T. A., Piskunov, N. E., Stempels, H. C., & Weiss, W. W. 2000, BaltA, 9, 590
Kurucz, R., & Bell, B. 1995, Atomic Line Data Kurucz CD-ROM No. 23 (Cambridge, MA: Smithsonian Astrophysical Observatory), 23
Leonard, D. C. 2007, ApJ, 670, 1275
Li, W., Bloom, J. S., Podsiadlowski, P., et al. 2011, Natur, 480, 348
Lind, K., Asplund, M., & Barklem, P. S. 2009, A&A, 503, 541
Livne, E., & Arnett, D. 1995, ApJ, 452, 62
Luck, R. E., & Heiter, U. 2007, AJ, 133, 2464
Matheson, T., Filippenko, A. V., Ho, L. C., Barth, A. J., & Leonard, D. C. 2000, AJ, 120, 1499
Mennekens, N., Vanbeveren, D., De Greve, J. P., & De Donder, E. 2010, A&A, 515, A89
Munari, U., Sordo, R., Castelli, F., & Zwitter, T. 2005, A&A, 442, 1127
Nugent, P. E., Sullivan, M., Cenko, S. B., et al. 2011, Natur, 480, 344
Oke, J. B., Cohen, J. G., Carr, M., et al. 1995, PASP, 107, 375
Pakmor, R., Kromer, M., Röpke, F. K., et al. 2010, Natur, 463, 61
Pan, K.-C., Ricker, P. M., & Taam, R. E. 2012a, ApJ, 760, 21
Pan, K.-C., Ricker, P. M., & Taam, R. E. 2012b, ApJ, 750, 151
Patat, F., Chandra, P., Chevalier, R., et al. 2007, Sci, 317, 924
Pietrinferni, A., Cassisi, S., Salaris, M., & Castelli, F. 2004, ApJ, 612, 168
Ramírez, S. V., & Cohen, J. G. 2002, AJ, 123, 3277
Reddy, B. E., Tomkin, J., Lambert, D. L., & Allende Prieto, C. 2003, MNRAS, 340, 304
Rest, A., Welch, D. L., Suntzeff, N. B., et al. 2008, ApJL, 681, L81
Reynoso, E. M., Moffett, D. A., Goss, W. M., et al. 1997, ApJ, 491, 816
Robin, A. C., Reylé, C., Derrière, S., & Picaud, S. 2003, A&A, 409, 523
Ruiter, A. J., Belczynski, K., & Fryer, C. 2009, ApJ, 699, 2026
Ruiz-Lapuente, P. 2004, ApJ, 612, 357
Ruiz-Lapuente, P., Comeron, F., Méndez, J., et al. 2004, Natur, 431, 1069
Saio, H., & Nomoto, K. 1985, A&A, 150, L21
Sim, S. A., Röpke, F. K., Hillebrandt, W., et al. 2010, ApJL, 714, L52
Simon, J. D., Gal-Yam, A., Gnat, O., et al. 2009, ApJ, 702, 1157
Sneden, C. 1973, ApJ, 184, 839
Sobeck, J. S., Kraft, R. P., Sneden, C., et al. 2011, AJ, 141, 175
Stefanik, R. P., Latham, D. W., & Torres, G. 1999, in ASP Conf. Ser. 185, IAU Colloq. 170, Precise Stellar Radial Velocities, ed. J. B. Hearnshaw & C. D. Scarfe (San Francisco, CA: ASP), 354
Sternberg, A., Gal-Yam, A., Simon, J. D., et al. 2011, Sci, 333, 856
Stetson, P. B., & Pancino, E. 2008, PASP, 120, 1332
Thompson, T. A., & Gould, A. 2012, arXiv:1210.6050
Tonry, J., & Davis, M. 1979, AJ, 84, 1511
Tucker, B. E. 2011, Ap&SS, 335, 223
Vogt, S. S., Allen, S. L., Bigelow, B. C., et al. 1994, Proc. SPIE, 2198, 362
Warren, J. S., Hughes, J. P., Badenes, C., et al. 2005, ApJ, 634, 376
Wilson, R. 1958, ApJ, 128, 57
Winkler, P. F., Gupta, G., & Long, K. S. 2003, ApJ, 585, 324
Yaron, O., & Gal-Yam, A. 2012, PASP, 124, 668
Yong, D., Lambert, D. L., Paulson, D. B., & Carney, B. W. 2008, ApJ, 673, 854
Yu, S., & Jeffery, C. S. 2010, A&A, 521, A85